Geophysical Journal International

Geophys. J. Int. (2018) **215,** 2071–2092
Advance Access publication 2018 September 20
GJI Geodynamics and tectonics

doi: 10.1093/gji/ggy393

Lithospheric 3-D flexural modelling of subducted oceanic plate with variable effective elastic thickness along the Manila Trench

Jiangyang Zhang,[1,2] Zhen Sun,[1] Min Xu,[1] Hongfeng Yang,[3] Yunfan Zhang[1] and Fucheng Li[1]

[1] *CAS Key Laboratory of Ocean and Marginal Sea Geology, Chinese Academy of Sciences, South China Sea Institute of Oceanology, Guangzhou* 510301, *China. E-mail: zhensun@scsio.ac.cn*
[2] *University of Chinese Academy of Sciences, Beijing* 100049, *China*
[3] *Earth System Science Programme, Faculty of Science, Chinese University of Hong Kong, Shatin, Hong Kong*

Accepted 2018 September 20. Received 2018 July 23; in original form 2018 January 15

SUMMARY

Flexural rigidity, indicated by the effective elastic thickness, is important for describing the mechanical behaviour of the subducted oceanic lithosphere in the thin plate model. 2-D thin plate models have been widely used in estimating the effective elastic thickness (T_e) of the oceanic lithosphere at subduction zones and collision zones. However, realistic lithospheric flexural modelling of the subducted oceanic plates should account for the lateral variation of T_e along the strike of the trench. We present a 3-D finite-difference flexural bending model that includes variable flexural parameters in all directions. We compare the results with 2-D flexural models, and we discuss the differences in estimating T_e within the bending plate at subduction zones. Theoretical analysis shows that when T_e changes only slightly along the trench, a 2-D model can sufficiently estimate T_e, when T_e changes sharply because of the effects of seamount loading and bending near the trench, tearing of the subducting plate, or the transition from subduction zone to collision zone; the T_e values calculated by 2-D models may produce errors up to 30 per cent compared with those predicted using a 3-D model, because they fail to account for the lateral slab-pulling force. We evaluate the differences between using 2-D and 3-D flexural model assumptions by simulating bending of the subducted oceanic plate at the northern Manila Trench. The results show that from the subduction zone to the collision zone, T_e estimated from the 2-D model gradually changes from 20.2 to 32.9 km, whereas T_e estimated from the 3-D model changes sharply at the continent–oceanic transition zone of the northern margin of the South China Sea.

Key words: Elasticity and anelasticity; Lithospheric flexure; Mechanics, theory, and modelling; Subduction zone processes.

1 INTRODUCTION

Generally, it is suggested that lithospheric rocks behave elastically or plastically over geologic time (i.e. $>10^6$ yr) and space scales (Turcotte & Schubert 2014), although numerous rheologies have been proposed for the mechanical behaviour of the oceanic lithosphere, such as perfectly plastic (Lobkovsky & Sorokhtin 1976), elastic-perfectly plastic (Turcotte *et al.* 1978), viscoelastic (Melosh 1978) and fully viscous behaviour (de Bremaecker 1977). The elastic thin plate theory has often been used to model the flexural shape of the lithosphere, especially the subducted oceanic plate (Hanks 1971; Watts & Talwani 1974; Parsons & Molnar 1976; Bodine & Watts 1979; McNutt 1984; McAdoo *et al.* 1985; McQueen & Lambeck 1989; Judge & McNutt 1991; Harris & Chapman 1994; Levitt & Sandwell 1995; Garcia-Castellanos *et al.* 2000; Bry & White 2007; Arredondo & Billen 2012; Zhang *et al.* 2014; Craig & Copley 2014; Craig *et al.* 2014; Emry *et al.* 2014; Zhou *et al.* 2015; Hunter & Watts 2016; Zhang *et al.* 2018; Zhou & Lin 2018). Some early studies on subducted oceanic plate flexure mainly focused on 2-D profiles along the dimension perpendicular to the trench using a uniform effective elastic thickness (T_e; Watts & Talwani 1974; Caldwell *et al.* 1976; Bodine & Watts 1979; Levitt & Sandwell 1995). Mounting evidence suggests that the bending of the oceanic plate produces normal faults near the outer rise during subduction (Christensen & Ruff 1988; Masson 1991; Kobayashi *et al.* 1998; Mortera-Gutiérrez *et al.* 2003; Ranero *et al.* 2003, 2005; Oakley *et al.* 2008; Lefeldt *et al.* 2012; Craig *et al.* 2014; Zhang *et al.* 2014, 2018; Emry & Wiens 2015; Zhou *et al.* 2015; Zhou & Lin 2018). These bending-related normal faults can cut several kilometres into the uppermost mantle and bring seawater into the crust and upper mantle, resulting in mantle serpentinization (Ranero *et al.* 2003; Grevemeyer *et al.* 2005). This process produces plate weakening and reduction in T_e near the trench axis, which indicates that a uniform T_e is unreasonable (McAdoo *et al.* 1985; Panteleyev & Diament 1993; Garcia-Castellanos *et al.* 2000; Billen & Gurnis 2005; Contreras-Reyes & Osses 2010; Craig & Copley 2014; Emry *et al.* 2014; Zhang *et al.* 2014, 2018; Zhou *et al.* 2015; Hunter & Watts 2016; Zhou & Lin 2018). Therefore, considering the yield envelope of the lithospheric rheology, McAdoo *et al.* (1985) proposed a layered rheology lithosphere (LRL) model, in which the plate was divided into three regimes: an upper brittle regime, a lower ductile regime, and an elastic regime sandwiched between the brittle and ductile layers. They further indicated that the LRL model was more practical than the elastic model. With a similar model (brittle–elastic–ductile), Panteleyev & Diament (1993) discussed the relative contributions of rheological parameters on lithospheric flexure in subduction zones. Garcia-Castellanos *et al.* (2000) developed a 2-D numerical algorithm with multilayered elastic–plastic rheology and reported a better fit to the bathymetry of the Tonga and Kermadec trenches than the classical homogeneous model. They then tested their model by comparing the predicted stress and yielding distributions with the outer-rise earthquake hypocentres in the subducting plate and found that they matched well. Emry *et al.* (2014) investigated earthquakes occurring during 1990–2011 around the southern and central/northern Mariana Trench and modelled the stress distribution of the subducting Pacific Plate with the method of Garcia-Castellanos *et al.* (1997). Their results showed that flexure models matched the location of extensional and compressional earthquakes. Craig & Copley (2014) indicated that T_e of oceanic lithosphere estimated by purely elastic plate modelling had little relationship with the plate age, because the purely elastic model may not represent the true rheology of the oceanic lithosphere. Zhou *et al.* (2015) studied the mechanisms of normal faults of the Mariana Trench and simulated the deformation of the subducting plate with a 2-D elastoplastic plate model based on the explicit Lagrangian method FLAC (Fast Lagrangian Analysis of Continua). They found that to fit the bathymetric profile and the structure of the normal faults, a horizontal tensional force was required. Zhou & Lin (2018) further indicated that bending-related normal faults reduced the T_e by nearly 52 per cent locally in the southern Mariana Trench and by 33 per cent in the central/northern region of the trench. As a simplification, Contreras-Reyes & Osses (2010) proposed a finite-difference solution of the 2-D flexural equation with variable T_e along the direction perpendicular to the trench and provided an effective method to estimate the trench-axis vertical loading force V_0, the trench-axis moment M_0, and T_e. They assumed that the reduction in T_e was a consequence of inelastic deformation. With a similar method to that of Contreras-Reyes & Osses (2010), Zhang *et al.* (2014) estimated the variation of T_e and other flexural parameters (M_0 and V_0) along the Mariana Trench and pointed out that the reduction in T_e varied from 21 to 61 per cent along the trench. Hunter & Watts (2016) used free-air gravity anomaly data to estimate T_e of circum-Pacific subducting oceanic lithosphere, based on a uniform T_e and a variable T_e, respectively. They found that the reduction in T_e was generally 40–65 per cent. In general, considering the yield strength of the lithosphere, two models are often used to investigate the flexural deformation of the lithosphere in subduction zones, the elastic–plastic model and the variable T_e elastic model, which both fit well with the bathymetry and free-air gravity anomaly data. Most studies have focused on the reduction of T_e in the direction perpendicular to the trench, although the results of Contreras-Reyes & Osses (2010) and Zhang *et al.* (2014) have shown that the T_e of the oceanic plate can vary not only in that direction but also along the strike of the trench. The 2-D flexural model generally fails to account for lateral variations of the flexural parameters and bending effects along the strike of the trench, which have been taken into account by 3-D flexural modelling in this study.

Realistic 3-D modelling of the flexural behaviour of the subducted oceanic lithosphere near the trench has been scarce until recently. Van Wees & Cloetingh (1994) first presented the finite-difference formulation for 3-D elastic flexure of the lithosphere, which was subsequently applied to investigate fault controlled 3-D basement geometries in Lake Tanganyika (East Africa). Wessel (1996) provided an analytical solution for 3-D flexural deformation of semi-infinite elastic plates with constant flexural rigidity. Braun *et al.* (2013) combined a 3-D flexural model (finite-difference method) with a thermal model (finite element method) of the underlying lithosphere to study complex passive margins. Manríquez *et al.* (2014) solved the flexure equations of the Reissner–Mindlin thin plate theory using the finite element method, and successfully applied it to study the Chile Trench. Garcia *et al.* (2015) reported an iterative spectral solution with variable rigidity. Most of the 3-D models discussed a finite area with fixed boundaries, which are unsuitable for dealing with subduction problems (van Wees & Cloetingh 1994; Braun *et al.* 2013; Arnaiz-Rodríguez & Audemard 2014).

The main question we attempt to address is whether it is accurate to use a 2-D thin plate to model the bending of the subducted lithosphere, especially when there is laterally variable T_e along the trench. In this study, we solved the 3-D flexural equations of the semi-infinite Kirchhoff plate using the finite-difference method (Fig. 1), focusing on the lateral variation in T_e of the flexural lithosphere and discussing the differences between 2-D and 3-D models in estimating flexural parameters of the subducted plate. The 3-D model was then applied to simulate the flexural shape of the northernmost region of the Manila Trench.

2 FLEXURAL MODEL

2.1 Basic equation

Considering a thin plate extending along two horizontal dimensions x and y, the plate's flexural rigidity $D(x, y)$ is only a spatially varying function (Garcia *et al.* 2015). Based on the Kirchhoff thin plate assumption, the differential equation governing the vertical deflection $w(x, y)$

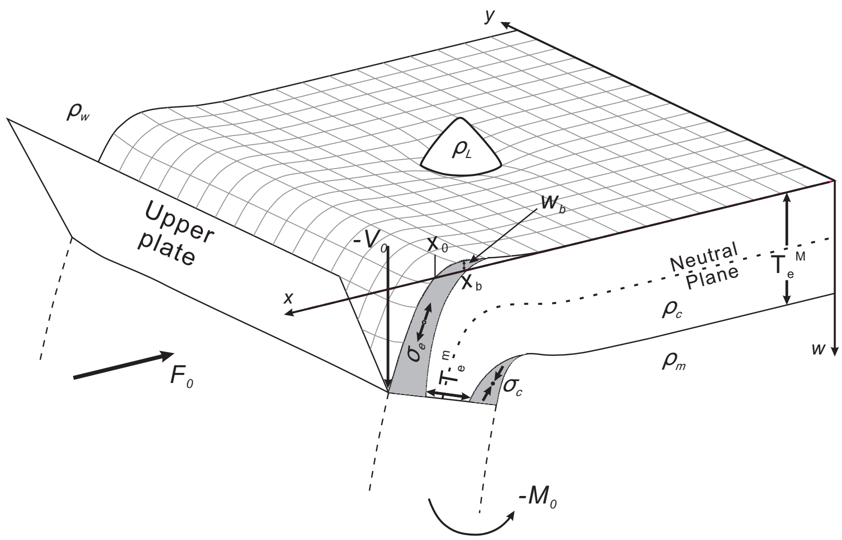

Figure 1. Diagram of the flexure produced by surface loading (seamount) and boundary loading. ρ_w, ρ_c and ρ_m are the densities of water, crust and mantle respectively; ρ_L is the applied load (seamount) density. M_0 is the bending moment, V_0 is the vertical shear force and F_0 is the horizontal force, which has been ignored in our model. T_e^M represents the seaward effective elastic thickness, and T_e^m is the bending-reduced effective elastic thickness

of an elastic plate with variable T_e is given by (van Wees & Cloetingh 1994; Braun *et al.* 2013):

$$\frac{\partial^2 D}{\partial x^2}\left(\frac{\partial^2 w}{\partial x^2}+\nu\frac{\partial^2 w}{\partial y^2}\right)+\frac{\partial^2 D}{\partial y^2}\left(\frac{\partial^2 w}{\partial y^2}+\nu\frac{\partial^2 w}{\partial x^2}\right)+2(1-\nu)\frac{\partial^2 D}{\partial x\partial y}\frac{\partial^2 w}{\partial x\partial y}+2\frac{\partial D}{\partial x}\left(\frac{\partial^3 w}{\partial x^3}+\frac{\partial^3 w}{\partial x\partial y^2}\right)+2\frac{\partial D}{\partial y}\left(\frac{\partial^3 w}{\partial y^3}+\frac{\partial^3 w}{\partial x^2\partial y}\right)$$
$$+D\left(\frac{\partial^4 w}{\partial x^4}+\frac{\partial^4 w}{\partial y^4}\right)+2D\frac{\partial^4 w}{\partial x^2\partial y^2}-N_x\frac{\partial^2 w}{\partial x^2}-2N_{xy}\frac{\partial^2 w}{\partial x\partial y}-N_y\frac{\partial^2 w}{\partial y^2}+\Delta\rho g w=q(x,y), \quad (1)$$

where $\Delta\rho = \rho_m - \rho_w$ is the density contrast between the mantle (ρ_m) and water (ρ_w) filling in the space created by the plate deflection $w(x, y)$; $q(x, y)$ is a spatially varying normal loading force, and N_x, N_y and N_{xy} represent in-plane forces. Tensile stresses are considered positive, whereas compressive stress is negative, following the definitions of Wessel (1996) and Garcia *et al.* (2015). The variable g is gravitational acceleration, and D is the flexural rigidity defined as:

$$D=\frac{ET_e^3(x,y)}{12(1-\nu^2)}, \quad (2)$$

where T_e is the effective elastic thickness, E is Young's modulus and ν is Poisson's ratio. Generally, ν is a constant, but T_e and E are allowed to vary spatially in this model. In addition, if the plate rigidity is uniform, eq. (1) would simplify to the biharmonic equation: $D\left(\frac{\partial^4 w}{\partial x^4}+\frac{\partial^4 w}{\partial y^4}\right)+2D\frac{\partial^4 w}{\partial x^2\partial y^2}-N_x\frac{\partial^2 w}{\partial x^2}-2N_{xy}\frac{\partial^2 w}{\partial x\partial y}-N_y\frac{\partial^2 w}{\partial y^2}+\Delta\rho g w=q(x,y)$. This equation has been given analytical solutions at various boundary conditions (Wessel 1996; Watts 2001). However, this equation assumes a constant D, and therefore cannot be used to solve the problem with variable T_e (D). In this study, eq. (1) must be solved numerically (finite-differences) because $q(x, y)$, D and T_e vary in an arbitrary manner in space. Therefore, according to the Kirchhoff thin plate assumption, the bending moment M_x, M_{xy} and M_y as well as the shear forces V_x and V_y become:

$$\begin{aligned}
M_x &= -D\left(\frac{\partial^2 w}{\partial x^2}+\nu\frac{\partial^2 w}{\partial y^2}\right)\\
M_y &= -D\left(\frac{\partial^2 w}{\partial y^2}+\nu\frac{\partial^2 w}{\partial x^2}\right)\\
M_{xy} &= -D(1-\nu)\frac{\partial^2 w}{\partial x\partial y}
\end{aligned} \quad (3)$$

and

$$\begin{aligned}
V_x &= -\frac{\partial D}{\partial x}\left(\frac{\partial^2 w}{\partial x^2}+\nu\frac{\partial^2 w}{\partial y^2}\right)-2(1-\nu)\frac{\partial D}{\partial y}\frac{\partial^2 w}{\partial x\partial y}-D\left[\frac{\partial^3 w}{\partial x^3}+(2-\nu)\frac{\partial^3 w}{\partial x\partial y^2}\right]-N_x\frac{\partial w}{\partial x}-2N_{xy}\frac{\partial w}{\partial y}\\
V_y &= -\frac{\partial D}{\partial y}\left(\frac{\partial^2 w}{\partial y^2}+\nu\frac{\partial^2 w}{\partial x^2}\right)-2(1-\nu)\frac{\partial D}{\partial x}\frac{\partial^2 w}{\partial x\partial y}-D\left[\frac{\partial^3 w}{\partial y^3}+(2-\nu)\frac{\partial^3 w}{\partial x^2\partial y}\right]-N_y\frac{\partial w}{\partial y}-2N_{xy}\frac{\partial w}{\partial x}.
\end{aligned} \quad (4)$$

The variables V_x and V_y contain the contributions from the twisting moments $\frac{\partial M_{xy}}{\partial y}$ and $\frac{\partial M_{xy}}{\partial x}$, which are called Kirchhoff's supplemented shear force (Timoshenko & Woinowsky-Krieger 1959). In addition, Hooke's Law of elastic bodies and the Kirchhoff assumptions of a thin plate assume: (1) the normal vectors to the middle surface are still orthogonal to the middle surface after deformation, (2) there is no strain in the direction perpendicular to the x–y plane, or $\varepsilon_{zz} = 0$ and (3) the middle surface has no strain parallel to the surface. The flexural stress field (σ_{xx}, σ_{yy} and σ_{xy}) is given by (Jin & Jiang 2002):

$$\begin{bmatrix} \sigma_{xx} \\ \sigma_{yy} \\ \sigma_{xy} \end{bmatrix} = \frac{E}{1+\nu} \begin{bmatrix} \frac{1-\nu}{1-2\nu} & \frac{\nu}{1-2\nu} & 0 \\ \frac{\nu}{1-2\nu} & \frac{1-\nu}{1-2\nu} & 0 \\ 0 & 0 & 1 \end{bmatrix} \begin{bmatrix} \varepsilon_{xx} \\ \varepsilon_{yy} \\ \varepsilon_{xy} \end{bmatrix} = -\frac{E}{1+\nu} \begin{bmatrix} \frac{1-\nu}{1-2\nu} & \frac{\nu}{1-2\nu} & 0 \\ \frac{\nu}{1-2\nu} & \frac{1-\nu}{1-2\nu} & 0 \\ 0 & 0 & 1 \end{bmatrix} \begin{bmatrix} \frac{\partial^2 w}{\partial x^2} \\ \frac{\partial^2 w}{\partial y^2} \\ \frac{\partial^2 w}{\partial x \partial y} \end{bmatrix} \tag{5}$$

where (ε_{xx}, ε_{yy}, ε_{xy}) represents the strain tensor. Compared with other 3-D finite-difference models with fixed boundaries, the domain of our model is a rectangle of length X and width Y with boundary conditions (Γ_1, Γ_2, Γ_3, Γ_4), listed as follows (Fig. 2):

$$\begin{aligned} &\Gamma_1 : \vec{M}_x = -\vec{M}_0, \vec{V}_x = -\vec{V}_0 \\ &\Gamma_2 : M_y = 0, V_y = 0 \\ &\Gamma_3 : w = 0, M_x = 0 \\ &\Gamma_4 : M_y = 0, V_y = 0. \end{aligned} \tag{6}$$

2.2 Finite-difference method

Based on the model shape, rectangular grids are used to divide the plate with regular node spacing dx and dy. With finite-difference approximations, eq. (1) can be replaced by differential equations. The continuum equation for each node is recast as a linear equation. The partial difference of D is directly evaluated, and deflection w is solved (van Wees & Cloetingh 1994). The large system of algebraic equations containing all nodes can be expressed as:

$$\mathbf{AW} = \mathbf{Q}, \tag{7}$$

where **A** is the coefficient matrix; **W** is the vector of unknown deflection w. The length of **W** is equal to the total number of nodes, and **Q** is a loading vector with the same length as **W** (the Appendix). The linear equations can be solved using Gaussian elimination or a multigrid, iterative method when the number of nodes is too large.

2.3 Extra loading and in-plane forces

The subducted oceanic lithosphere may not be subjected only to the trench-axis vertical loading, and axial bending moment, but also to surface loadings from features such as seamounts or sediments and horizontal loading from slab pull, ridge push or plate interface coupling. This finite-difference method allows $q(x, y)$ to vary arbitrarily in both the x and y directions, and therefore it differs from the previous flexural models assuming $q(x) = 0$ (Caldwell *et al.* 1976; Parsons & Molnar 1976; Levit & Sandwell 1995; Kemp & Stevenson 1996; Chang *et al.* 2012; Craig & Copley 2014; Turcotte & Schubert 2014), as well as the flexural model with $q(x)$ only changing in the direction perpendicular to the trench (McAdoo *et al.* 1985; Panteleyev & Diament 1993; Garcia-Castellanos *et al.* 2000; Billen & Gurnis 2005; Contreras-Reyes & Osses 2010; Craig & Copley 2014; Emry *et al.* 2014; Zhang *et al.* 2014; Zhou *et al.* 2015; Hunter & Watts 2016; Zhang *et al.* 2018; Zhou & Lin 2018). The horizontal in-plane forces were set to zero in some previous studies (van Wees & Cloetingh 1994; Contreras-Reyes & Osses 2010; Zhang *et al.* 2014; Hunter & Watts 2016; Zhang *et al.* 2018), as researchers suggested that these values will only cause the onset of buckling when they reach critical values and it is too difficult to produce such great stresses at subduction zones. However, more and more research has shown that the in-plane force cannot be ignored (Karner 1983; Karner *et al.* 1993; Muller *et al.* 1996; Garcia-Castellanos *et al.* 2000; Craig & Copley 2014; Emry *et al.* 2014; Zhou *et al.* 2015; Zhou & Lin 2018). Garcia-Castellanos *et al.* (2000) reported that the horizontal force in the Tonga and Kermadec trenches reached 4.0–10.0 $\times$ 10^{12} N m^{-1}, which had the same order of magnitude as the axis vertical force. Zhou *et al.* (2015) studied the mechanism of normal faulting in the Marina Trench and reported a horizontal tensional force of 2.4–4.8 $\times$ 10^{12} N m^{-1}. Note that horizontal in-plane forces are included in our model by the terms N_x, N_y and N_{xy} in eq. (1).

2.4 3-D inversion method

In the 3-D model, the boundary loadings M_0 and V_0 are vectors rather than single values, and T_e becomes a 2-D matrix. Because there are too many inversion parameters for conventional analysis, parameter vectors are searched by particle swam optimization (PSO method; Shi & Eberhart 1998). As the distance between the initial solution space and the optimum solution affects the convergence time, we used 2-D inversion results to help constrain the initial solution space of the 3-D inversion. The 3-D inversion results are displayed in Figs 3 and 4.

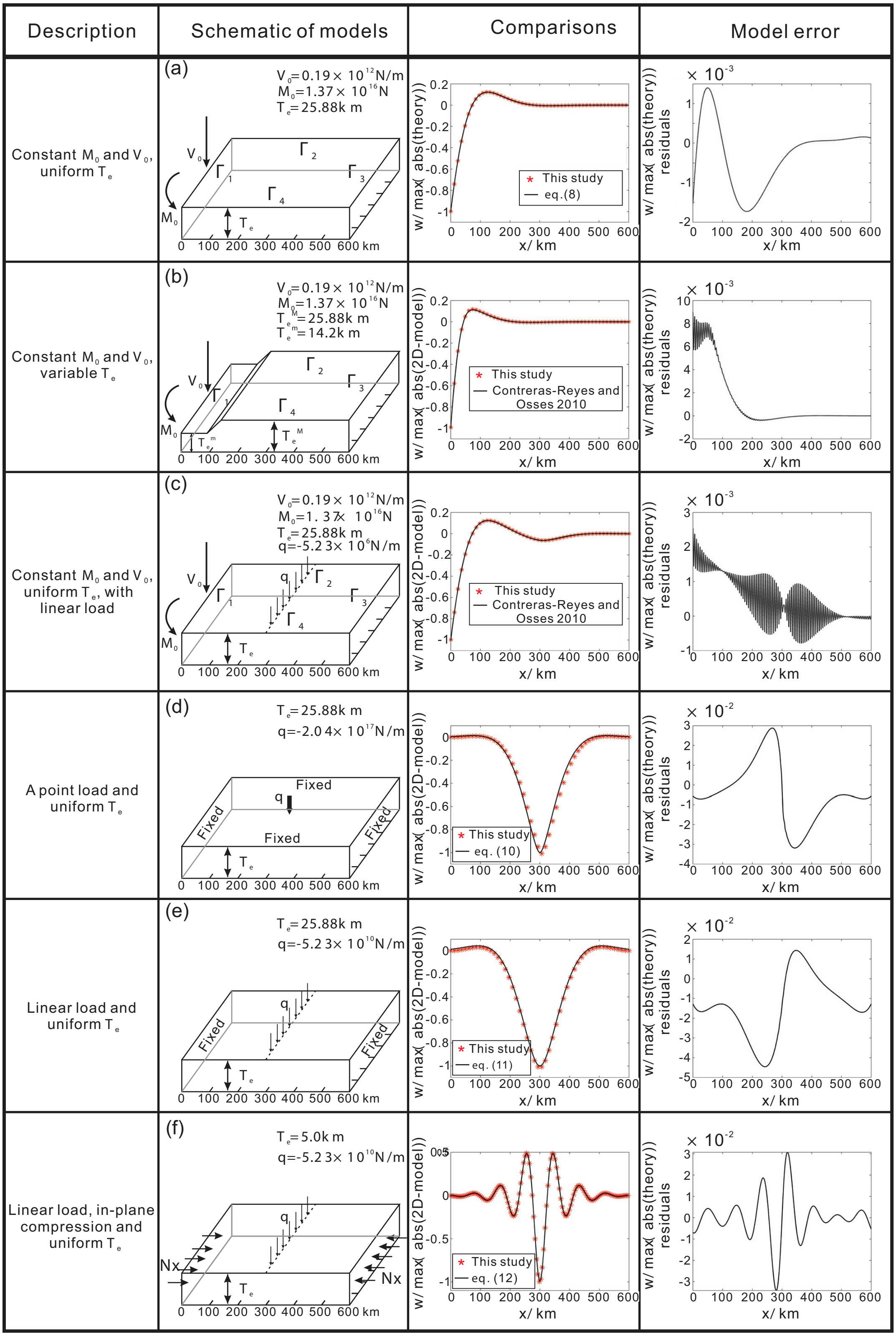

Figure 2. Comparisons between our 3-D model, analytic solutions, and a 2-D finite difference model (Contreras-Reyes & Osses 2010). (a) Comparisons between our model and the 2-D analytic solution with boundary load and uniform T_e. (b) Comparisons between our model and the 2-D model of Contreras-Reyes & Osses (2010) with boundary loading and variable T_e. (c) Comparisons between our model and the 2-D model of Contreras-Reyes & Osses (2010) with boundary loading and surface loading. (d) Comparisons between our model and the 2-D analytic solution with a point load and uniform T_e, (e) Comparisons between our model and the 2-D analytic solution with linear load and uniform T_e. (f) Comparisons between our model and the 2-D analytic solution with linear load, in-plane compression, and uniform T_e.

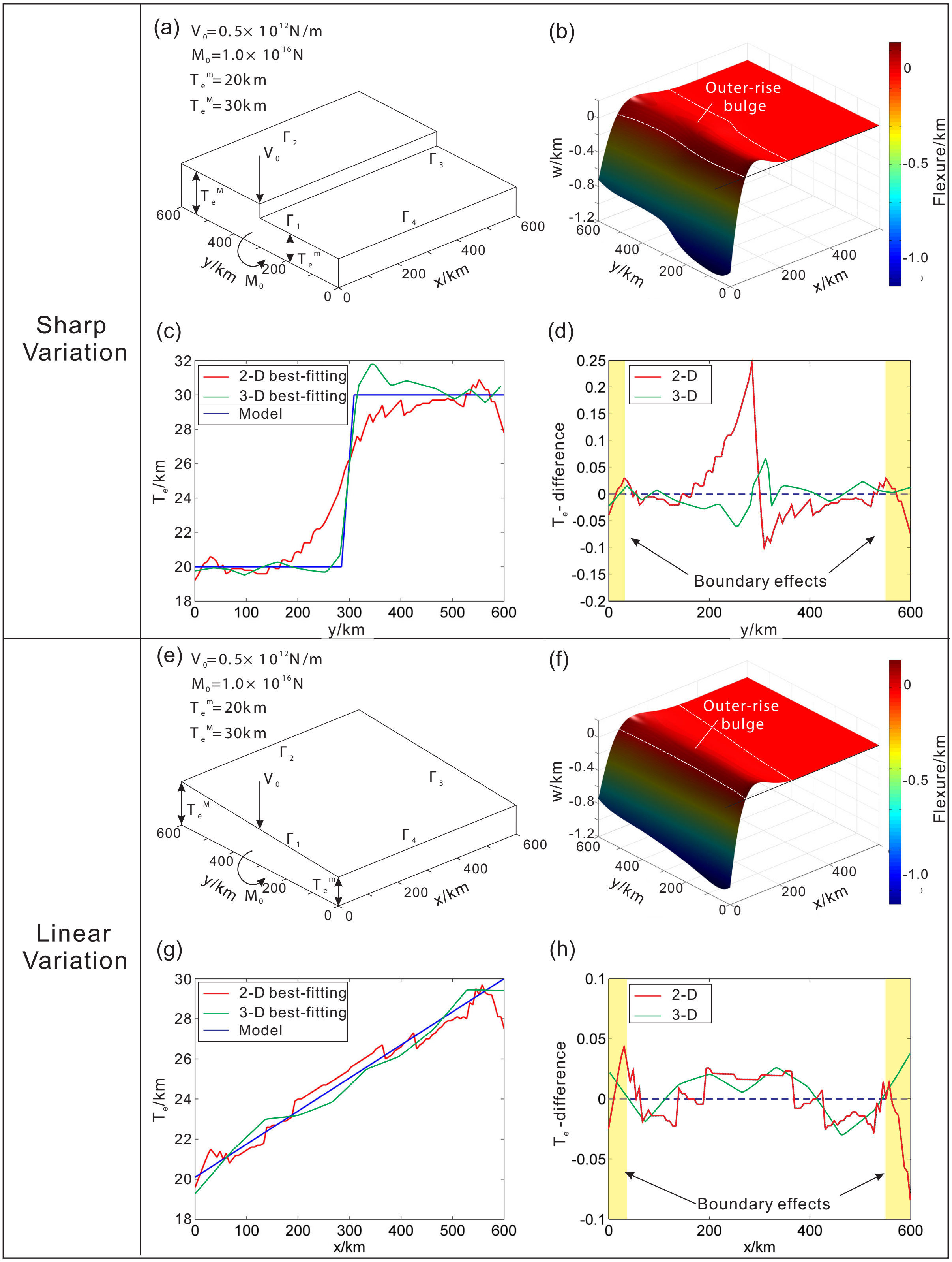

Figure 3. The difference between T_e estimated by a 2-D and a 3-D model, with laterally sharp and linearly variable T_e. (a) 3-D models with boundary conditions, (b) 3-D forward results, (c and d) the difference between T_e estimated by 2-D and 3-D inversion results and the initial model.

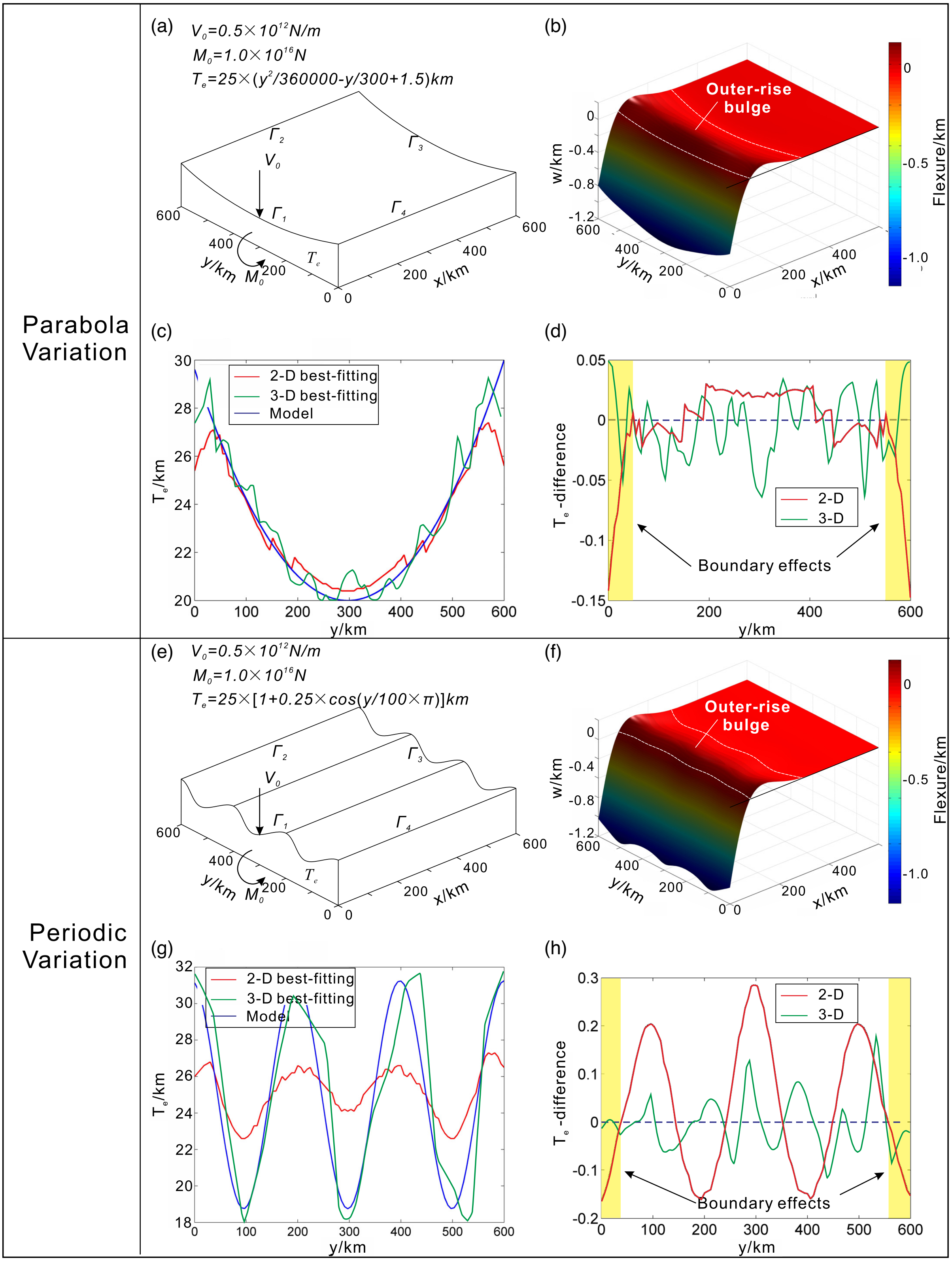

Figure 4. The difference between T_e estimated by a 2-D and a 3-D model with a lateral parabola and periodic variable T_e. (a) 3-D models with boundary conditions, (b) 3-D forward results, (c and d) the difference between T_e estimated by 2-D and 3-D inversion results and the initial model.

Table 1. Constants and parameters used in the flexure model.

Symbol	Description	Value	Unit
E	Young's modulus	7×10^{10}	Pa
g	Acceleration due to gravity	9.81	m s^{-2}
ν	Poisson's ratio	0.25	
ρ_m	Mantle density	3300	kg m^{-3}
ρ_c	Crust density	2700	kg m^{-3}
ρ_s	Sediment density	2000	kg m^{-3}
ρ_w	Water density	1030	kg m^{-3}

3 COMPARISON OF 2-D AND 3-D FLEXURAL MODELLING

3.1 Validation of the 3-D model

Comparisons between finite-difference solutions and analytical solutions have been performed for point loads (van Wees & Cloetingh 1994; Braun *et al.* 2013), line loads and disc loads (van Wees & Cloetingh 1994). Here, to test the accuracy of our 3-D flexural modelling of a subducted oceanic plate, the numerical solutions were compared with the 2-D analytical solution under a simple case describing the flexural response of an elastic plate to an end vertical shear force V_0 and an end bending moment M_0 with a uniform T_e (Fig. 2). However, for tests with varying T_e and extra loading, no analytical solutions were available. We therefore compared our 3-D flexural modelling results with a 2-D finite-difference model, which was previously used to estimate the flexural parameters of the Chile Trench (Contreras-Reyes & Osses 2010) and the Mariana Trench (Zhang *et al.* 2014). We then compared out 3-D flexural modelling results with the 3-D analytical solution under point loading, the 2-D analytical solution under line loading, and the 2-D analytical solution under horizontal force as well as surface line loading, respectively. The constants and parameters used for the numerical simulation are listed in Table 1. We tested our finite-difference model with a grid spacing 3 km $\times$ 3 km within a model space of 600 km $\times$ 600 km (the same setup used in the other simulations in this paper).

The comparison results are summarized in Fig. 2. The left-hand panel of the Figure shows different model schematics with flexural parameters and boundary conditions. The middle panel shows a comparison of calculated normalized deflections between the solutions in this study and other solutions. The solid black lines represent the analytical solution or 2-D finite-difference solutions, and the red star points indicate our 3-D model solutions. The right-hand panel shows the differences between our solutions and the other solutions; these differences are on the order of $\sim 10^{-3}$ times smaller than the calculated values, which indicate that they are negligible (Fig. 2).

3.1.1 Constant M_0 and V_0 with uniform T_e

The 2-D analytical solution for the deflection w of uniform T_e under a bending moment M_0 and an end loading V_0 is given by (Turcotte & Schubert 2014):

$$w = \frac{\alpha^2 e^{-x/\alpha}}{2D}\left[-M_0 \sin\left(\frac{x}{\alpha}\right) + (V_0\alpha + M_0)\cos\left(\frac{x}{\alpha}\right)\right] \quad (8)$$

where the flexural parameter α is defined by:

$$\alpha = \left(\frac{4D}{\Delta\rho g}\right)^{1/4}. \quad (9)$$

The vertical force and bending moment are the result of the gravitational body force acting on the descending plate (Turcotte & Schubert 2014). In this test, the boundary conditions are showed in eq. (6) and Fig. 2(a). In addition, we assume an end vertical shear force $V_0 = 0.19 \times 10^{12}$ N m^{-1}, an end bending moment $M_0 = 1.37 \times 10^{16}$ N, and a uniform $T_e = 25.88$ km. These values are taken from profile P06 of Contreras-Reyes & Osses (2010), and are appropriate for oceanic lithosphere. The comparison results indicate that our 3-D model can achieve very high accuracy with model error of no more than 0.2 per cent (Fig. 2a).

3.1.2 Constant M_0 and V_0 with variable T_e

For the case of variable T_e with constant M_0 and V_0, no analytical solutions are available. We therefore compared our 3-D model with the 2-D finite-difference model of Contreras-Reyes & Osses (2010). The values of V_0 and M_0 are the same as the values shown in Fig. 2(a), whereas T_e changes from 25.88 km (the T_e seaward of the outer rise: $T_e{}^M$) to 14.2 km (the T_e landward of the outer rise: $T_e{}^m$) according to profile P06 of Contreras-Reyes & Osses (2010) (Fig. 2b). The reduction of T_e in the trench outer-rise region is commonly considered to be related to a fractured and hydrated lithosphere as well as to bending-related faults (Christensen & Ruff 1988; Ranero *et al.* 2003; Contreras-Reyes *et al.* 2008a).

In addition, previous studies suggested that the bending-relate faults could continue to grow as the plate moves toward the trench (e.g. Zhou *et al.* 2015). The reduction of T_e was thus assumed to be linear rather than to change suddenly, which may be more similar to reality.

This comparison indicates that the results of our 3-D model differ by less than 1 per cent from those of the 2-D finite-difference model of Contreras-Reyes & Osses (2010) (Fig. 2b).

3.1.3 Constant M_0 and V_0 with uniform T_e and linear load

For the third validation of the 3-D model, M_0, V_0 and T_e are the same as the values shown in Fig. 2(a). An extra line load $q = -5.23 \times 10^6$ N m–1 was applied over the elastic plate in this model. The results of this comparison suggest that the model match is excellent, and there are only minor differences near the trench and the position of the line loads (Fig. 2c). Again, the model error indicates that the difference between our 3-D model results and those of the 2-D finite-difference model are less than 1 per cent (Fig. 2c).

3.1.4 Point loading with uniform T_e

The problem of point loading on the plate is best addressed with axisymmetric solutions. The analytical solution for the deflection w of a plate under a point load q with a uniform T_e is given by (Turcotte & Schubert 2014):

$$w = \frac{q\alpha^2}{2\pi D} kei\left(\frac{r}{\alpha}\right), \tag{10}$$

where the function *kei* is a Bessel–Kelvin function of zero order (Abramowitz & Stegun 1970), q is the point load that is a function only of r, and r represents the cylindrical radius or the radial coordinate in the plane of the plate. In this test, the fixed boundary conditions were set as shown in Fig. 2(d). The point load q is equal to 5.67×10^9 N m^{-1}, and T_e is equal to 25.88 km. The model error is less than 4 per cent (Fig. 2d).

3.1.5 Linear loading and uniform T_e

Bending of the lithosphere under the loads of island chains has been observed in many areas, such as the Hawaiian Ridge (Watt 1978) and the Louisville Ridge (Lyons *et al.* 2000). The analytical solution of deflection under linear loading is given by (Turcotte & Schubert 2014):

$$w = \frac{V_0\alpha^3}{8D} e^{-x/\alpha}\left(\cos\frac{x}{\alpha} + \sin\frac{x}{\alpha}\right), \tag{11}$$

where V_0 is the applied linear load, equal to 8.72×10^8 N m^{-1}. As before, T_e is set to 28.55 km. Fig. 2(e) shows that the model error is no more than 5 per cent (Fig. 2e).

3.1.6 Linear loading, in-plane compression and uniform T_e

The last benchmark is linear loading on a uniform T_e plate, with an additional constant compressional in-plane force N_{xx} applied along the x-axis. The analytical solution is given by (Hetenyi 1946):

$$w = -w_e e^{(-|x|/\beta)}\left[\beta\cos\left(\frac{x}{\gamma}\right) + \gamma\sin\left(\frac{|x|}{\gamma}\right)\right], \tag{12}$$

where $w_e = V_0/2\alpha^2\Delta\rho g$, β and γ are the flexural parameters, which are expressed as:

$$\beta = \left[\left(\frac{\Delta\rho g}{4D}\right)^{1/2} + \left(\frac{N_x}{4D}\right)\right]^{-1/2} \tag{13}$$

$$\gamma = \left[\left(\frac{\Delta\rho g}{4D}\right)^{1/2} - \left(\frac{N_x}{4D}\right)\right]^{-1/2}. \tag{14}$$

We can identify the critical buckling load N_c from the form of β and γ: $N_c = 2(\Delta\rho g D)^{1/2}$. Here, the compressional in-plane force is set $0.95N_c$, and T_e is set to 5 km. The numerical model differs from the analytic formula by no more than 3 per cent (Fig. 2g).

All the three validation tests show a perfect match between our 3-D model and the analytic solution and the 2-D finite-difference models, which indicates that our 3-D model should accurately simulate the flexural response of a subducted oceanic plate to most loadings.

3.2 Comparison of 2-D and 3-D models with laterally variable T_e

Eq. (8) shows that the analytical solution of the shape of a bending oceanic plate at the trench is determined by T_e, M_0 and V_0. Unfortunately, M_0 and V_0 cannot be independently measured. A practical way to calculate the T_e, M_0 and V_0 simultaneously is to identify the best-fitting free-air gravity anomaly (Bry & White 2007; Hunter &Watts 2016) or the bathymetric profile (Garcia-Castellanos *et al.* 2000; Bry & White 2007; Contreras-Reyes & Osses 2010; Emry *et al.* 2014; Zhang *et al.* 2014). However, most 2-D flexural model simulations have ignored the lateral variations in flexural parameters, such as T_e. Here, we performed four different experiments to analyse the difference between 2-D and 3-D flexural models in estimating the T_e. The T_e was set to sharp, linear, parabolic and periodic variation, respectively, along the dimension parallel to the trench, separately and in advance (Fig. 3); $V_0 = 0.5 \times 10^{12}$ N m^{-1} and $M_0 = 1.0 \times 10^{16}$ N. All finite-difference models used a grid spacing 3 km × 3 km within a model space of 600 km × 600 km. The boundary conditions are also shown in Fig. 3.

Initially, we applied the same end loading on different experiments and simulated the 3-D flexural deformation. Furthermore, 200 evenly distributed deformation profiles perpendicular to the trench were extracted from the 3-D model and regarded as the 'observed flexures', which were then fitted using the 2-D flexure method following Bry & White (2007) and a 3-D inversion method. Finally, we checked the difference between the 2-D and 3-D inversion results and the 3-D models in estimating T_e. The results are displayed in Figs 3(c), (g) and 4(c), (g). The blue line represents the pre-set T_e used in the 3-D model, the red line is 2-D best-fitting T_e, and the green line is the 3-D inversion result. The difference is shown as a percentage between the 2-D and 3-D best-fitting models, and the pre-set T_e is shown in Figs 3(d), (h) and 4(d), (h).

In Figs 3(a)–(d), the T_e is set to vary sharply from 20 to 30 km along the strike of the trench, and Fig. 3(a) provides a schematic of the loading configuration. Please note that x is the direction of subduction, and boundary condition 1 (Γ_1) therefore represents the 'trench'. Fig. 3(b) shows that under these boundary loadings, the deflection of the plate changes from nearly −1400 m to nearly −800 m gradually rather than suddenly, as there is interaction (V_y and M_{xy}) within the plate along the y direction. This interaction generally causes the difference between the 2-D and 3-D flexural model results in estimating T_e (as previous 2-D models usually ignored this interaction). In addition, the distances from the outer-rise bulge to the trench increase gradually with T_e changing from 20 to 30 km. In Figs 3(c) and (d), the results suggest that the difference between 2-D inverted T_e and the initial model can reach nearly 25 per cent at the place where T_e changes suddenly, whereas the difference between 3-D inverted T_e and the initial model is under 5 per cent.

In Figs 3(e)–(h), T_e changes from 20 to 30 km along the strike of the trench with linear variation. The deflections change from nearly −1065 m to nearly −825 m linearly, and the distances from the outer-rise bulge to the trench also change linearly. In addition, both T_e differences of the 2-D and 3-D results are relatively small (under 3 per cent; Figs 3g and h).

In Figs 4(a)–(d), the elastic thickness changes in the shape of a parabola: $T_e = 25 \times (y^2/360\,000 - y/300 + 1.5)$ km. Under these end loadings, the shape of the deflections and the distances from the outer-rise bulge to the trench are both similar to a parabola (Fig. 4b). The T_e difference of the 2-D model is closed to 3 per cent, whereas the T_e difference of the 3-D model is a little larger (nearly 5 per cent; Figs 4c and d).

In Figs 4(e)–(h), the elastic thickness is set to a periodic variation with $T_e = 25 \times [1 + 0.25\cos(y\pi/100)]$ km. Both the deflections and the distances from the outer-rise bulge to the trench therefore change periodically (Fig. 4f). However, unlike the previous groups of experiments, the T_e difference of the 2-D model can reach nearly 30 per cent here, whereas the T_e difference of the 3-D model is around 15 per cent (Figs 4g and h).

These results show that 3-D inversion obtains a relatively high accuracy to estimate the T_e of the bending plate, especially when sharp lateral variation in T_e exists.

3.3 The difference between 2-D and 3-D models in estimating the T_e

After employing dozens of different calculation models, we found that the ratio of the variation in T_e wavelength to the flexural wavelength of the plate can affect the accuracy of estimated T_e using a 2-D model. The flexural wavelength of a thin plate is given by: $L_p = 2\pi\alpha$. Fig. 5(a) illustrates this relationship: L is the sharp variation distance of T_e (from T_e^a to T_e^b; T_e^b is equal to half of T_e^a here), which represents the variation wavelength of T_e here. Our experimental results show that the relation between the maximum T_e difference and the T_e wavelength variation ratio to the flexural wavelength of the plate ($L/2\pi\alpha$, α calculated using T_e^a here) can be approximated as a power function (Fig. 5b). Thus, the faster the T_e changes along-strike, the less accurate the 2-D plate model.

This phenomenon also demonstrates that a simple oceanic lithosphere scenario with a gentle change of T_e can be reasonably modelled using a 2-D approximation. However, for complex geological settings with laterally variable flexural parameters (M_0, V_0 and T_e), the transition from subduction zone to collision zone, or at the subduction of continent–ocean transition, the 2-D model no longer applies.

4. FLEXURAL MODELLING OF THE NORTHERNMOST MANILA TRENCH

4.1 Geological setting

The Manila Trench, located at the east of the South China Sea (SCS), was formed by the subduction of the Eurasian Plate underneath the Philippine Sea Plate (Bowin *et al.* 1978; Taylor & Hayes 1983; Hayes & Lewis 1984). A characteristic feature of this convergent boundary is a gradual change from normal subduction in the south to a collisional regime in the north that produces the Taiwan orogeny. GPS data suggest that the Philippine Sea Plate is moving to the northwest at the rate of 71 mm yr^{-1} (Seno *et al.* 1993), and the convergence rate between the Eurasian Plate and central Luzon varies from 20 to 100 mm yr^{-1} (Fig. 6; Galgana *et al.* 2007). The interpreted timing of seafloor spreading in the northern SCS based on magnetic anomaly data suggests that the continent–ocean boundary intersects the Manila Trench at ∼19°N (yellow dashed line shown in Fig. 6, Briais *et al.* 1993). However, multichannel seismic (MCS) reflection imaging suggests that the intersection of the continent–ocean boundary and the Manila Trench is at ∼20°N (Eakin *et al.* 2014). The Taiwan Mountain Belt, which is the northward

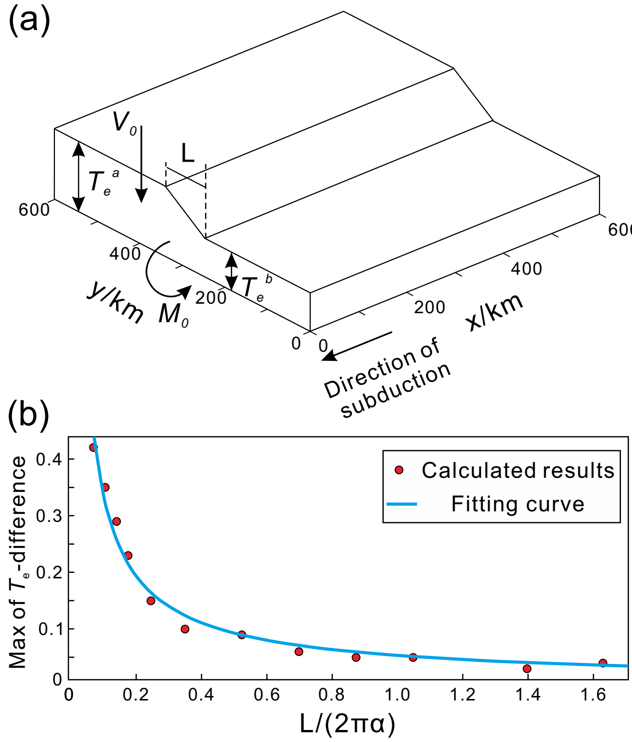

Figure 5. (a) Schematic diagram of a 3-D model with a lateral variable of effective elastic thickness. *L* represents the sharp variation with distance of T_e (from T_e^a to T_e^b, where T_e^b is equal to half of T_e^a). (b) Plotting maximum of T_e difference versus $L/(2\pi\alpha)$, where α is the flexural parameter of T_e^a.

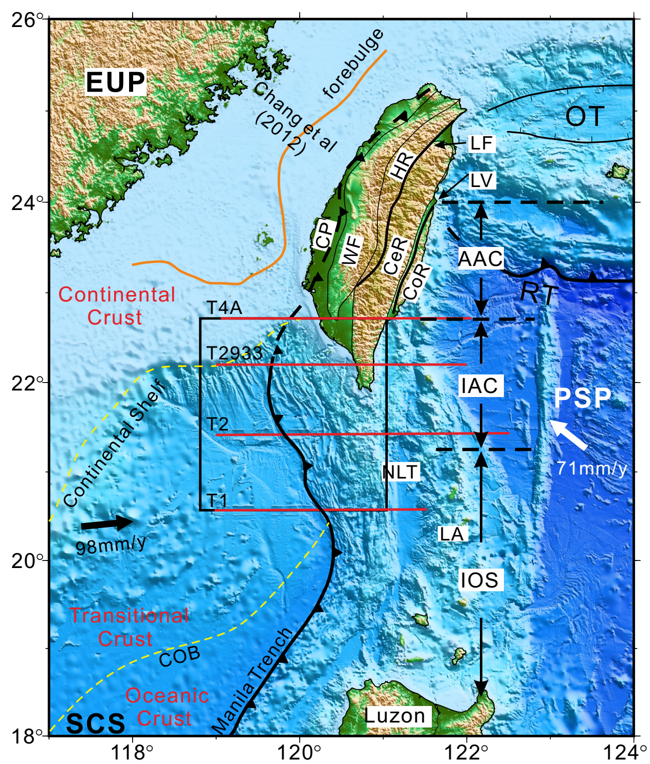

Figure 6. Tectonic setting of the study area and the locations of the seismic profiles. Yellow dashed lines represent the continental shelf and COB, which divide the subducted plate into continental, transitional, and oceanic crust. The orange line is the edge of the forebulge from Lin & Watts (2002). EUP—Eurasian Plate; PSP—Philippine Sea Plate; CP—coastal plain; WF—Western Foothills; HR—Hsueshan Range; CeR—Central Range; CoR—Coastal Range; LF—Lishan fault; LV—Longitudinal valley; RT—Ryukyu Trench; OT—Okinawa Trench; IOS—Intra-oceanic subduction; IAC—Initial arc-continent collision; and AAC—advanced arc-continent collision (from Huang *et al.* 2000). The convergence rates and direction along the Manila Trench are from Rangin *et al.* (1999) and Seno *et al.* (1993).

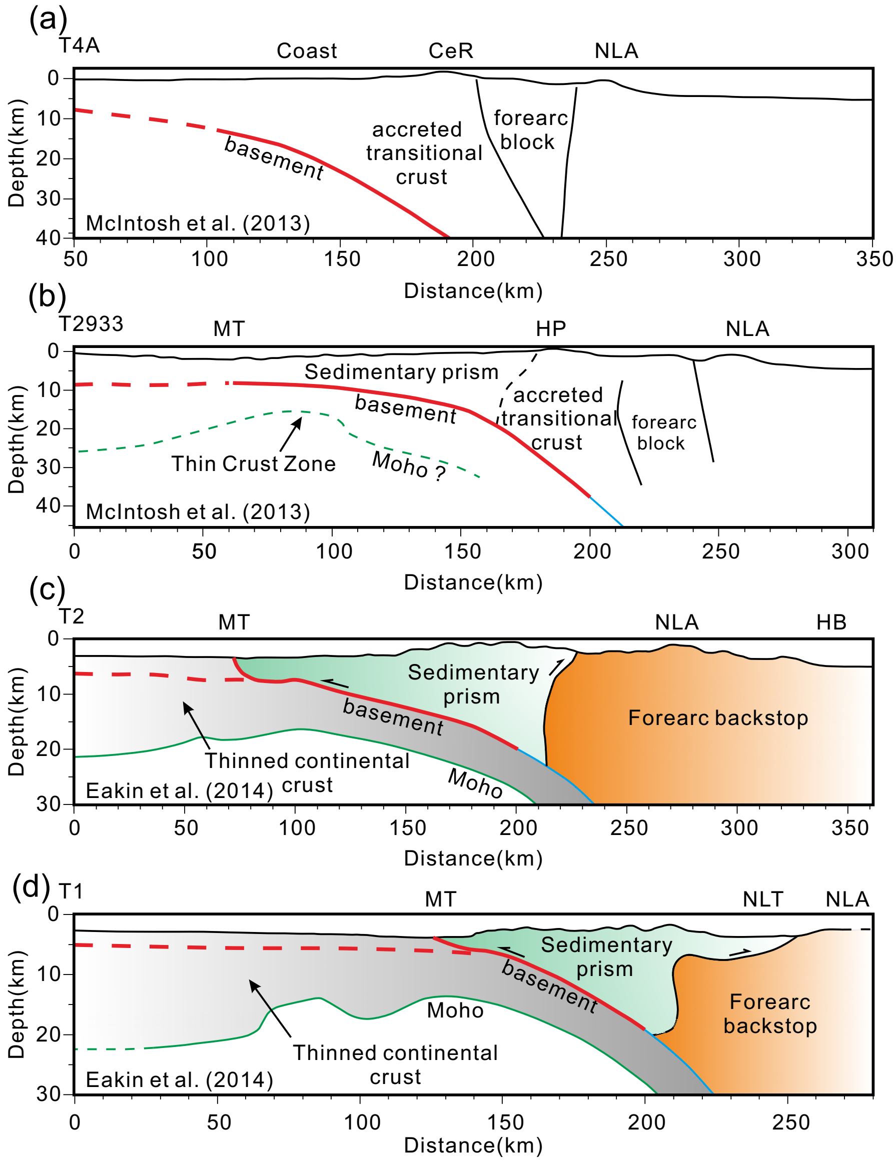

Figure 7. Crustal structure of the northern Manila Trench and Taiwan collision zone. (a) Crustal structure of transect T4A from McIntosh *et al.* (2013). NLA—North Luzon Arc. Note that the profile starts from 50 km. (b) Crustal structure of transect T2933 from McIntosh *et al.* (2013). MT—Manila Trench. HP—Hengchun Peninsula. (c) Crustal structure of transect T2 from Eakin *et al.* (2014). HB—Huatung Basin. (d) Crustal structure of transect T1 from Eakin *et al.* (2014). NLT—North Luzon Trough.

extension of the Manila Trench, began to form in the Mid-Miocene and was uplifted following arc–continent collision in the last 6.5 Ma. The geological and geophysical features of the Taiwan arc–continent collision indicate that it can be divided into four geodynamic processes: intraoceanic subduction (south of 21°20′N); initial arc–continent collision (21°20′–22°40′N), advanced arc–continent collision (22°40′–24° N); and arc collapse/subduction (24°–24°30′N; Huang *et al.* 2000; Fig. 6).

Recently, several wide-angle seismic profiles were acquired across the northernmost Manila Trench, at the transition zone from subduction (south) to collision (north) (Figs 7a–d) (McIntosh *et al.* 2013; Eakin *et al.* 2014). The velocity structure profiles across southern Taiwan, at ∼22.7°N (T4A in Fig. 7a), and the Hengchun Peninsula of southernmost Taiwan, at ∼22.2°N (T2399 in Fig. 7b), indicate that the crustal thickness is ∼9–15 km (McIntosh *et al.* 2013). The velocity structure profiles of the incipient arc–continent collision (T2 and T1 in the Fig. 6) suggest that it extends to hyperextended continental crust (∼10–15 km thick; Figs 7c and d), and a multichannel seismic (MCS) reflection image shows subduction of normal oceanic crust south of ∼22°N (Eakin *et al.* 2014). These velocity structure profiles suggest that the tectonic setting varies from the Manila Trench to the Taiwan arc–continent collision zone from south to north. The crust of the Eurasian Plate thickens from oceanic crust to transitional crust and then to continental crust. Although T_e has little correlation with any geological or physical boundary within the lithosphere (McNutt *et al.* 1988; Bechtel *et al.* 1990), these crustal structure variations can help constrain the flexural morphology of the subducted plate when estimating T_e. In addition, based on comparison with bathymetric profiles, seismic profiles

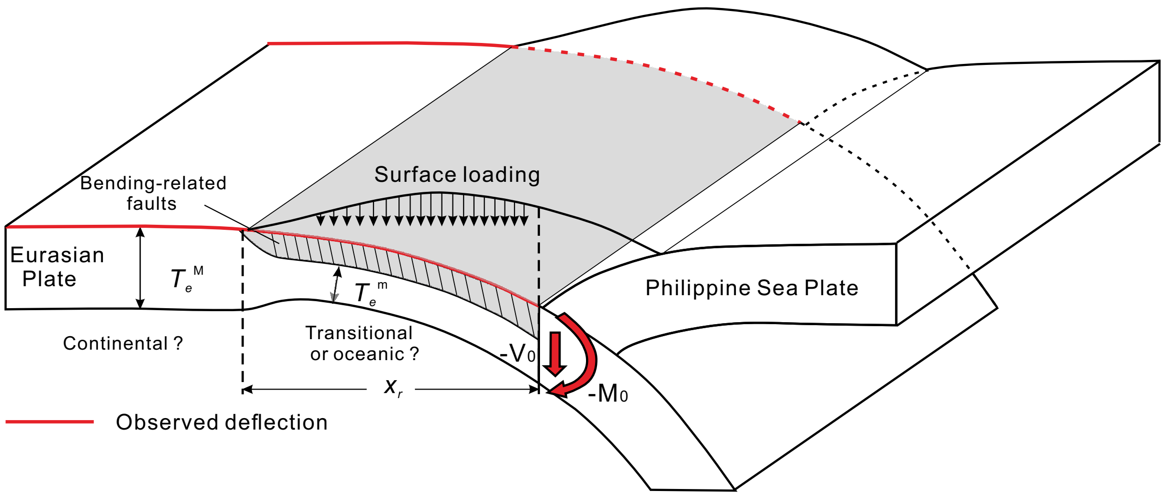

Figure 8. Schematic diagram of the 3-D flexural models of the Manila Trench and Taiwan collision zone (modified from Wang & Lee 2011; Zhang *et al.* 2014). T_e^M and T_e^m are two characteristic values of effective elastic thickness. T_e^M is the effective elastic thickness where the plate curvature is negligible, and T_e^m is the effective elastic thickness that is reduced because of inelastic deformation (faults) or variable crustal thickness. The red line represents the observed deflection of the subducted plate. The effects of surface loading and boundary loading ($-V_0$ and $-M_0$) are both considered.

can help minimize the interference of sediments, especially in areas with thick deposits. Thick sedimentary deposits can make the trench depth shallow, and thus result in bathymetry (and even gravity data) that cannot reflect the deflection of the lithosphere.

In this study, we simulate these bending morphologies using 2-D and 3-D models respectively, assuming the flexural parameters listed in Table 1. The basement morphologies of the four parallel profiles (T1, T2, T2933 and T4A) were extracted as the input for our flexural modelling (basements indicated by solid red lines in Figs 7a-d). In contrast from the previous 2-D flexural models of the Manila Trench (Chang *et al.* 2012) and Central Taiwan (Lin & Watts 2002; Mouthereau & Petit 2003; Tensi *et al.* 2006; Wang & Lee 2011), our 3-D model accounts for both surface loading (accretionary wedge or mountain) and subsurface loading (boundary bending moment and vertical force) (Fig. 8). To avoid edge effects, the 3-D model dimensions comprise a rectangular area between profiles T1 and T4A, shown in Fig. 6, and has been suitably extended to the west with a length of 400 km, similar to Wang & Lee (2011). Along the dimension parallel to the trench (collision zone), boundary loads $M_0(y)$, $V_0(y)$ can change arbitrarily. For simplicity, we assigned values to four special nodes of M_0 (y) and $V_0(y)$, which corresponds to the four profiles (T1, T2, T2933 and T4A). Values of other nodes were interpolated from the four special nodes.

4.2 Model results

The 2-D model results shown in Fig. 9 suggest that from the Manila Trench to the Taiwan collision zone, T_e^M ranges from 20.2 to 32.9 km, and T_e^m ranges from 8.5 to 28.6 km. The T_e of continental crust is greater than that of transitional and oceanic crust at the Manila Trench. The 3-D model results show a similar trend in T_e (Fig. 10). However, the 3-D model suggests sharp variation of T_e^M in the area between profiles T2 and T2933 (21°30′–22°N), which cannot be captured by the 2-D model (Fig. 10b). This sharp variation of T_e^M corresponds to the continent–ocean transition of the northern margin of the SCS.

Furthermore, we found that using a continuous 3-D model to fit the bending profiles T2 and T2933 at the same time, we must add an upward vertical force at the plate boundary in profile T2 (Fig. 10a). Otherwise, the plate along the profile T2 would be pulled downward by the lateral force induced from profile T2933. This finding may imply that inelastic deformation existed in the area between the profiles T2 and T2933, such as plate tearing or viscous deformation. Another possible reason is that a subducted buoyant plateau was present in this area (Fan *et al.* 2016).

4.3 Discussion

4.3.1 The in-plane force in the Manila Trench

Many studies have shown that the in-plane force is an important parameter when estimating T_e (Karner 1986; Karner *et al.* 1993; Mueller *et al.* 1996; Garcia-Castellanos *et al.* 2000; Craig & Copley 2014; Emry *et al.* 2014; Zhou *et al.* 2015; Zhou & Lin 2018). Karner (1983) indicated that the in-plane force played a role in modifying plate rigidity. A tensile in-plane force increases plate rigidity, whereas a compressive in-plane force decreases plate rigidity. Garcia-Castellanos *et al.* (2000) found that to minimize the mean difference between the calculated and observed bathymetry in the Tonga and Kermadec trenches, a tensile horizontal force was needed to increase the deflection of the plate and reduce the amplitude of the outer rise (forebulge) simultaneously. Our numerical tests shows that a compressive horizontal force could increase the amplitude of the outer rise (forebulge) (Fig. 2f). The seismic profile across the Western Taiwan Foreland Basin shows a regional

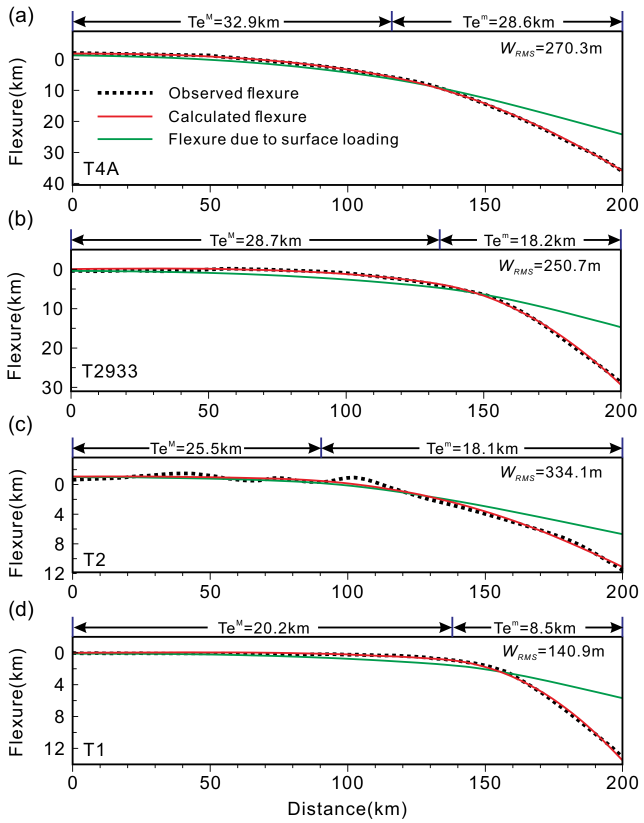

Figure 9. Comparison of the simulated and observed flexure of the subducted Eurasian Plate in response to surface loading and boundary loading ($-M_0$ and $-V_0$). The black dotted line represents the observed deflection (red parts in Figs 6b–e), the green lines are calculated deflection only due to surface loading, and the red lines are calculated deflection due to surface loading, bending moment ($-M_0$) and shear force ($-V_0$).

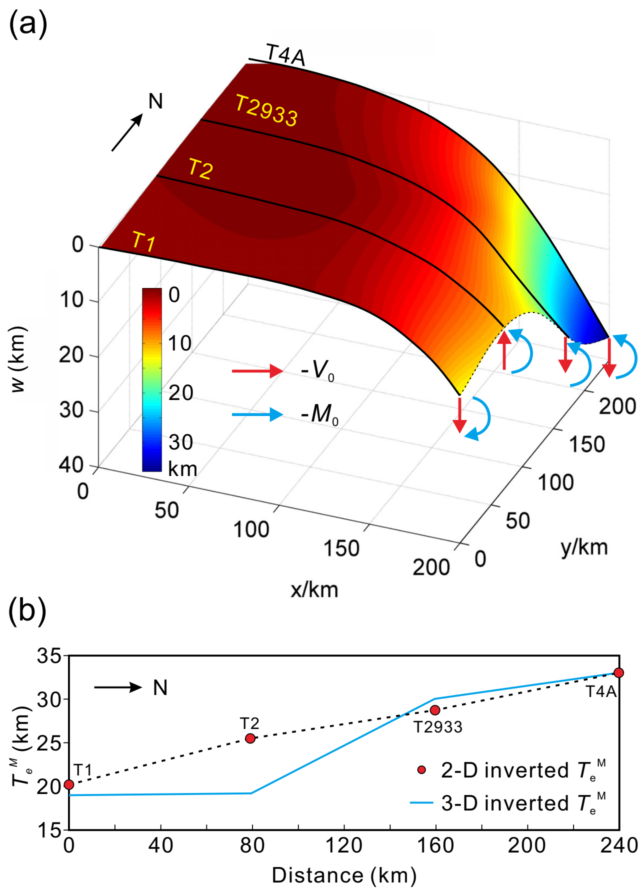

Figure 10. (a) 3-D simulated result. We must add an upward vertical force at the plate boundary in profile T2. (b) T_e^M inverted by 2-D model (red circles) and 3-D model (blue line).

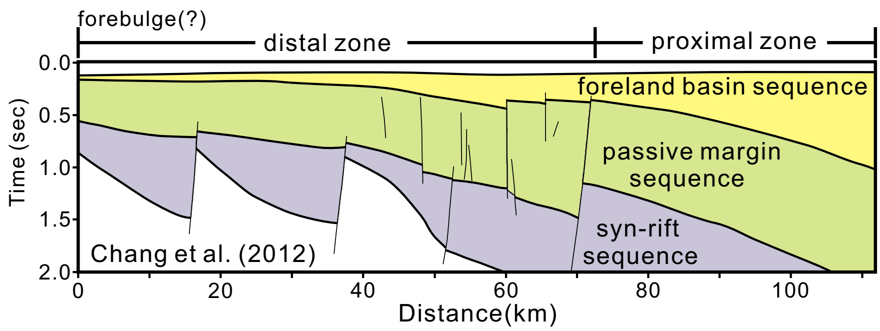

Figure 11. Seismic interpretation profile across the Western Taiwan Foreland Basin (Chang *et al.* 2012) (the location is shown in Fig. 6). The forebulge here may result from the compressive horizontal force produced by collision between the Luzon arc and the Chinese continental margin.

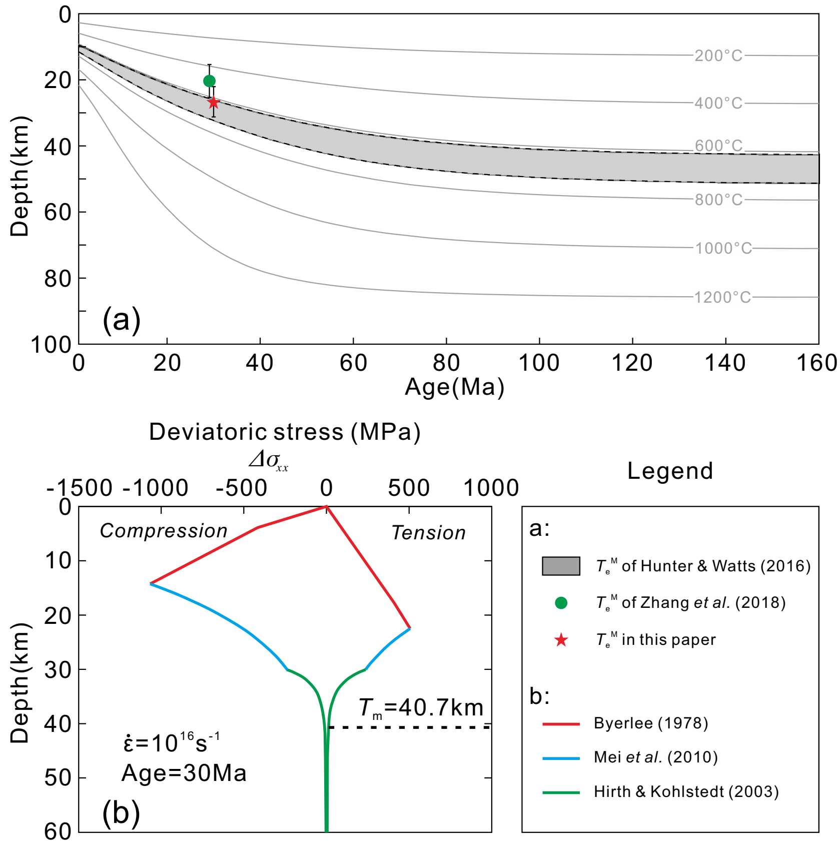

Figure 12. (a) Comparison of T_e^M in this paper (red star) and Zhang *et al.* (2018) (green circle) and Hunter & Watts (2016) (grey area) at ∼30 Ma. The grey curves show the depth to the plate-cooling isotherms of Parsons & Sclater (1977). (b) The YSE used by Hunter & Watts (2016) which is a combination of the rheology laws of Byerlee (1978) (red lines), Mei *et al.* (2010) (blue lines), and Hirth & Kohlstedt (2003) (green lines). At 30 Ma, the T_m is nearly 40.7 km, which is larger than the T_e^M at the same age.

unconformity, which is the result of regional uplift of the forebulge due to the loading of the Taiwan orogen, erosion, and subsequent migration of the forebulge (Figs 6 and 11; Chang *et al.* 2012). We infer that the compressive horizontal force produced by collision between the Luzon arc and the Chinese continental margin is a main factor for the formation of the forebulge. However, in the northern Manila Trench, no apparent forebulge is observed in the seismic profiles (Figs 7a–d). Thus, a tensile horizontal force may be applied on the subducted plate, just as in the cases of the Tonga and Kermadec trenches (Garcia-Castellanos *et al.* 2000). Another possible interpretation is that the crustal heterogeneity of the continent–ocean boundary hinders the propagation of the flexural wave and reshapes the morphology of the damping wave from theoretical expectations (Chang *et al.* 2012).

4.3.2 The rheology of the lithosphere and seismicity

Goetze & Evans (1979) suggested that the yield strength envelope (YSE) derived from experimental rock mechanics data could be used to predict T_e. This predicted T_e in turn can help to evaluate rheological parameters and test the predictions of laboratory-derived flow laws

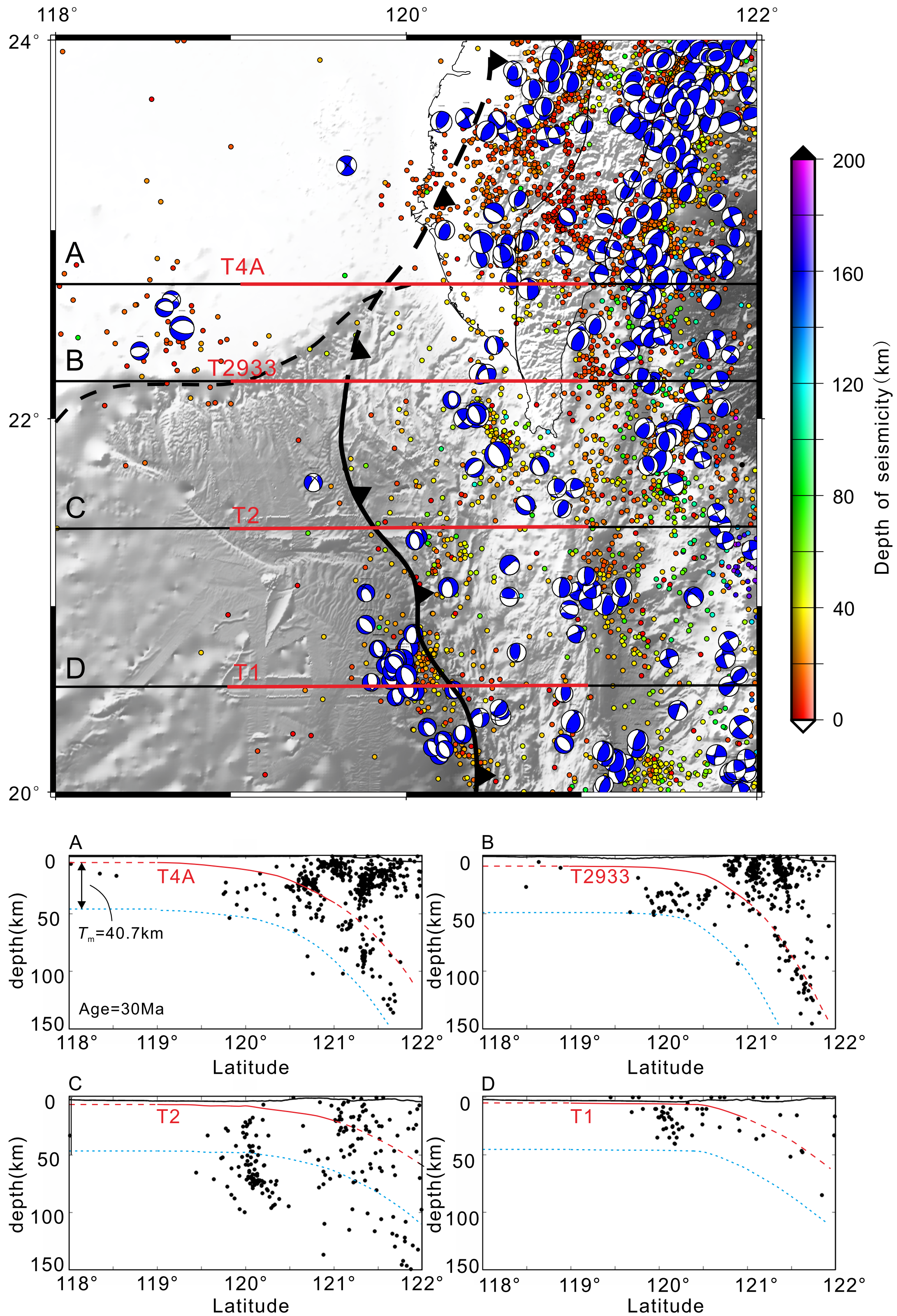

Figure 13. Seismicity (data from ISC) and focal mechanisms (data from the Global CMT project data catalogue) of the northernmost Manila Trench. A, B, C and D are profiles along the four OBS profiles. The red lines are the basement extracted from OBS profiles, red dashed lines represent the basement inferred from the seismicity, and the blue dotted lines represent the calculated bottom of the mechanical layer ($T_{\rm m}$ = 40.7 km at 30 Ma based on a YSE similar to that of Hunter & Watts 2016).

(Panteleyev & Diament 1993; Hunter & Watts 2016). Hunter & Watts (2016) estimated the T_e of circum-Pacific subduction zones using a uniform T_e model and a variable T_e model, respectively. By comparing the observed T_e based on the elastic model to the predicted T_e based on different YSEs and the ε elastic–perfectly plastic model, they found that both the landward T_e and the seaward T_e increased with oceanic plate age, following the 342 ± 22 and 671 ± 55 °C oceanic isotherms based on a cooling plate model, respectively. They then indicated that the low-temperature plasticity (LTP) flow laws of Goetze (1978), Evans & Goetze (1979), Raterron *et al.* (2004) and Mei *et al.* (2010) all showed good fits with the estimated T_e of circum-Pacific subduction zones (assuming a constant strain rate 10^{16} s^{-1}). Along the strike of the northernmost Manila Trench, both $T_e{}^M$ and $T_e{}^m$ increase with plate age, which is consistent with the results of Hunter & Watts (2016). The oceanic lithosphere mechanical thickness (T_{mo}) is 40.7 km at ~30 Ma based on the YSE similar to that of Hunter & Watts (2016) [a combination of the rheology laws of Byerlee (1978), Mei *et al.* (2010) and Hirth & Kohlstedt (2003); Fig. 12b]. Here, T_{mo} represents the depth at which the yield strength falls below 1 per cent of the overburden pressure (Hunter & Watts 2016). The mechanical thickness of the continental lithosphere (T_{mc}) of the Western Taiwan Foreland Basin is 40–50 km (Mouthereau & Petit 2003). However, the $T_e{}^M$ in this area is only 26.8 ± 4.6 km (from ~20 to 33 km), which is similar to the $T_e{}^M$ of circum-Pacific subduction zones at ~30 Ma (Based on Hunter & Watts 2016, $T_e{}^M$ varied from 26.1 to 32.3 km), and a little larger than $T_e{}^M$ of Zhang *et al.* (2018) (20.3 ± 5.0 km; Fig. 12a). This value is much smaller than T_m (T_{mo} and T_{mc}), which suggests that these flow lows are too strong to fit the observations. We infer that this discrepancy may be owing to two reasons. One is that a great deal of magmatic activity occurred during the spreading of the SCS (Fan *et al.* 2017), which may have changed the thermal structure of the lithosphere and thus the rheological structure. Another possible reason is that the YSE of continent–ocean transition may be more complex than that of the oceanic lithosphere. Therefore, it is not appropriate to constrain the deformation mechanism of the continent–ocean transition based on a simple rheological flow law of the oceanic lithosphere.

Seismicity is frequently associated with brittle deformation in the lithosphere. Mouthereau & Petit (2003) investigated the rheological structure and distribution of crustal earthquakes in the Western Taiwan Foreland Basin, and found that most earthquakes depths were less than 15 km. In contrast, at the outer rise of the Manila Trench, the depth of seismicity was more than 50 km (Fig. 13). The seismicity profiles show that the slab dip increases from south to north (slab dip changes from ~24° to ~55°; Fig. 13). This great change in slab dip over such a short distance also implies that the subducted plate may be discontinuous in the area between 21°N and 22°N.

5 CONCLUSION

The 3-D flexural method presented herein is applicable to convergent belts such as subduction and collision zones. The 3-D model was compared with a simpler 2-D formulation to estimate the T_e of subducting lithosphere. We presented a case study for bending at the northernmost region of the Manila Trench. The following conclusions were reached. (1) When simulating the bending of oceanic lithosphere at subduction zones, where T_e changes smoothly in general, the 2-D model is similar to the 3-D model and can be used where the deviation in T_e is less than 5 per cent. However, for the area where sharp variation of T_e exists, such as at the transition from the subduction zone to the collision zone, the 3-D model better recreates the abrupt change along-strike. (2) The T_e of the subducting lithosphere may change sharply at the northern margin of the SCS. We propose that this change may result from the non-uniform deformation of the subducted plate, and/or subducted plate tearing.

ACKNOWLEDGEMENTS

We are grateful to Jian Lin, Di Zhou, Ning Qiu and Cuimei Zhang for useful discussion. We thank Zhongxian Zhao, Fan Zhang and Zhiyuan Zhou for offering technical assistance. GMT (Wessel and Smith 1998) was used to draw the topographic map. This research was funded by the Joint Program of the National Science Foundation of China (NSFC) and Guangdong Province (No. U1301233), a Guangdong NSF research team project (2017A030312002) and the NSFC (No. 41206040, 41576070).

REFERENCES

Abramowitz, M. & Stegun, I.A., 1970. *Handbook of Mathematical Functions,* 9th edn, Dover Publications, Inc.

Arnaiz-Rodríguez, M.S. & Audemard, F., 2014. Variations in elastic thickness and flexure of the Maracaibo block, *Journal of South American Earth Sciences,* **56,** 251–264.

Arredondo, K.M. & Billen, M.I., 2012. Rapid weakening of subducting plates from trench-parallel estimates of flexural rigidity, *Phys. Earth planet. Inter.,* **196,** 1–13.

Bechtel, D., Forsyth, D.W., Sharpton, V.L. & Grieve, R.A.F., 1990. Variations in effective elastic thickness of the North American lithosphere, *Nature,* **343,** 636–638.

Billen, M.I. & Gurnis, M., 2005. Constraints on subducting plate strength within the Kermadec trench, *J. geophys. Res.* **110,** B05407.

Bodine, J.H. & Watts, A.B., 1979. On lithospheric flexure seaward of the Bonin and Mariana trenches, *Earth planet. Sci. Lett.* **43,** 132–148.

Bowin, C., Lu, R.-S., Lee, C.-S. & Schouten, H., 1978. Plate convergence and accretion in Taiwan-Luzon region, *AAPG Bull,* **62,** 1645–1672.

Braun, J., Deschamps, F., Rouby, D. & Dauteuil, O., 2013. Flexure of the lithosphere and the geodynamical evolution of non-cylindrical rifted passive margins: Results from a numerical model incorporating variable elastic thickness, surface processes and 3D thermal subsidence, *Tectonophysics,* **604,** 72–82.

Briais, A., Patriat, P. & Tapponnier, P., 1993. Updated interpretation of magnetic anomalies and seafloor spreading stages in the South China Sea: implications for the tertiary tectonics of Southeast Asia, *J. geophys. Res.*, **98**(B4), 6299–6328.

Bry, M. & White, N., 2007. Reappraising elastic thickness variation at oceanic trenches, *J. geophys Res.,* **112**(B8).

Byerlee, J., 1978. Friction of rocks, *Pure appl. Geophys.,* **116**(4–5), 615–626.

Caldwell, J.G., Haxby, W.F., Karig, D.E. & Turcotte, D.L., 1976. On the applicability of a universal elastic trench profile, *Earth planet. Sci. Lett.,* **31,** 239–246.

Chang, J.-H., Yu, H.-S., Lee, T.-Y., Hsu, H.-H., Liu, C.-S. & Tsai, Y.-T., 2012. Characteristics of the outer rise seaward of the Manila Trench and implications in Taiwan–Luzon convergent belt, South China Sea, *Mar. Geophys. Res.,* **33,** 351–367.

Christensen, D.H. & Ruff, L.J., 1988. Seismic coupling and outer rise earthquakes, *J. geophys. Res.,* **93,** 13 421–13 444.

Contreras-Reyes, E., Grevemeyer , I., Flueh, E.R. & Reichert, C., 2008a. Upper lithospheric structure of the subduction zone offshore southern Arauco Peninsula, Chile at ˜38°S, *J. geophys. Res.,* **113,** B07303.

Contreras-Reyes, E. & Osses, A., 2010. Lithospheric flexure modeling seaward of the Chile trench: implications for oceanic plate weakening in the Trench Outer Rise region, *Geophys. J. Int.,* **182**(1), 97–112.

Craig, T.J. & Copley, A., 2014. An explanation for the age independence of oceanic elastic thickness estimates from flexural profiles at subduction zones, and implications for continental rheology. *Earth planet. Sci. Lett.,* **392,** 207–216.

Craig, T.J., Copley, A. & Jackson, J., 2014. A reassessment of outer-rise seismicity and its implications for the mechanics of oceanic lithosphere, *Geophys. J. Int.,* **197**(1), 63–89.

de Bremaecker, J.C., 1977. Is the oceanic lithosphere elastic or viscous?, *J. geophys. Res.,* **82**(14), 2001–2004.

Eakin, D.H., McIntosh, K.D., Van Avendonk, H.J.A., Lavier, L., Lester, R., Liu, C.-S. & Lee, C.-S., 2014. Crustal-scale seismic profiles across the Manila subduction zone: the transition from intra-oceanic subduction to incipient collision, *J. geophys. Res.,* **119,** 1–17.

Emry, E.L. & Wiens, D.A., 2015. Incoming plate faulting in the Northern and Western Pacific and implications for subduction zone water budgets, *Earth planet. Sci. Lett.,* **414,** 176–186.

Emry, E.L., Wiens, D.A. & Garcia-Castellanos, D., 2014. Faulting within the Pacific plate at the Mariana Trench: implications for plate interface coupling and subduction of hydrous minerals, *J. geophys. Res.,* **119,** 3076–3095.

Evans, B. & Goetze, C., 1979. The temperature variation of hardness of olivine and its implication for polycrystalline yield stress, *J. geophys. Res.,* **84**(B10), 5505–5524.

Fan, C.-Y., Xia, S.-H., Zhao, F., Sun, J.-L., Cao, J.-H., Xu, H.-L. & Wan, K.-Y., 2017. New insights into the magmatism in the northern margin of the South China Sea: Spatial features and volume of intraplate seamounts, *Geochem. Geophys. Geosyst.,* **18**(6), 2216–2239.

Fan, J., Zhao, D.-P & Dong, D.-D., 2016. Subduction of a buoyant plateau at the Manila Trench: tomographic evidence and geodynamic implications. *Geochem. Geophys. Geosyst.,* **17,** 1–16.

Galgana, G., Hamburger, M., McCaffrey, R., Corpuz, E. & Chen, Q., 2007. Analysis of crustal deformation in Luzon, Philippines using geodetic observations and earthquake focal mechanisms, *Tectonophysics,* **432,** 63–87.

Garcia-Castellanos, D., Fernàndez, M. & Torne, M., 1997. Numerical modeling of foreland basin formation: a program relating thrusting, flexure, sediment geometry and lithosphere rheology, *Computers & Geosciences,* **23,** 993–1003.

Garcia-Castellanos, D., Torne, M. & Fernàndez, M., 2000. Slab pull effects from a flexural analysis of the Tonga and Kermadec trenches (Pacific Plate), *Geophys. J. Int.,* **141**(2), 479–484.

Garcia, E.S., Sandwell, D.T. & Luttrell, K.M., 2015. An iterative spectral solution method for thin elastic plate flexure with variable rigidity, *Geophys. J. Int.,* **200**(2), 1010–1026.

Goetze, C., 1978. The mechanisms of creep in olivine [and discussion], *Phil. Trans. R. Soc. Lond. A, Math. Phys. Sci.,* **288**(1350), 99–119.

Goetze, C. & Evans, B., 1979. Stress and temperature in the bending lithosphere as constrained by experimental rock mechanics, *Geophys. J. Int.,* **59,** 463–478.

Grevemeyer, I., Kaul, N., Diaz-Naveas, J.L., Villinger, H., Ranero, C.R. & Reichert, C., 2005. Heat flow and bending-related faulting at subduction trenches: case studies offshore of Nicaragua and Central Chile, *Earth planet. Sci. Lett.,* **236,** 238–248.

Hanks, T.C., 1971. The Kuril trench–Hokkaido Rise system: large shallow earthquakes and simple models of deformation, *Geophys. J. Int.,* **23,** 173–189.

Harris, R. & Chapman, D., 1994. A comparison of mechanical thickness estimates from trough and seamount loading in the southeastern Gulf of Alaska. *J. geophys. Res.,* **95,** 9297–9317.

Hayes, D. E. & Lewis, S.D., 1984. A geophysical study of the Manila Trench, Luzon, Philippines: 1. Crustal structure, gravity, and regional tectonic evolution, *J. geophys. Res.,* **89,** 9171–9195.

Hetenyi, M., 1946. *Beams on Elastic Foundation: Theory with Applications in the Fields of Civil and Mechanical Engineering,* The University of Michigan Press.

Hirth, G. & Kohlstedt, D., 2003. Rheology of the upper mantle and the mantle wedge: a view from the experimentalists, in *Inside the Subduction Factory,* pp. 83–105, ed. Eiler, J., American Geophysical Union.

Huang, C.-Y., Yuan, P.-B., Lin, C.-W., Wang, T.-K. & Chang, C.-P., 2000. Geodynamic processes of Taiwan arc-continent collision and comparison with analogs in Timor, Papua New Guinea, Urals and Corsica, *Tectonophysics,* **325,** 1–21.

Hunter, J. & Watts, A.B., 2016. Gravity anomalies, flexure and mantle rheology seaward of circum-Pacific trenches, *Geophys. J. Int.,* **207**(1), 288–316.

Jin, Y. & Jiang, X.D., 2002. *Lithosphere Dynamics,* 1st edn, Science Press, Beijing, p. 231.

Judge, A.V. & McNutt, M.K., 1991. The relationship between plate curvature and elastic plate thickness: a study of the Peru-Chile Trench, *J. geophys. Res.,* **96**(B10), 16625–16639.

Karner, G.D., 1983. Effects of lithospheric in-plane stress on sedimentary basin stratigraphy, *Tectonics,* **5,** 573–588.

Karner, G.D., Driscoll, N.W. & Weissel, J.K., 1993. Response of the lithosphere to in-plane force variations, *Earth planet. Sci. Lett.,* **114,** 397–416.

Kemp, D.V. & Stevenson, D.J., 1996. A tensile, flexural model for the initiation of subduction, *Geophys. J. Int.,* **125,** 73–94.

Kobayashi, K., Nakanishi, M., Tamaki, K. & Ogawa, Y., 1998. Outer slope faulting associated with the western Kuril and Japan trenches, *Geophys. J. Int.,* **134,** 356–372.

Lefeldt, M., Ranero, C.R. & Grevemeyer, I., 2012. Seismic evidence of tectonic control on the depth of water influx into incoming oceanic plates at subduction trenches, *Geochem.Geophys.Geosyst,* **13,** 1–17.

Levitt, D.A. & Sandwell, D.T., 1995. Lithospheric bending at subduction zones based on depth soundings and satellite gravity, *J. geophys. Res.,* **100**(B1), 379–400.

Lin, A.T. & Watts, A.B., 2002. Origin of the West Taiwan basin by orogenic loading and flexure of a rifted continental margin, *J. geophys. Res.,* **107**(B9), ETG 2–1-ETG 2-19.

Lobkovsky, L.I. & Sorokhtin, O.G, 1976. Plastic deformation of oceanic lithosphere in a subduction zone, in *Tectonics of Lithospheric Plates,* pp. 22–52, ed. Sorokhtin, O.G., Institutes Okeanologii Akad. Nauk SSSR.

Lyons , S.N., Sandwell , D.T. & Smith , W.H.F, 2000. Three-dimensional estimation of elastic thickness under the Louisville Ridge, *J. geophys. Res.,* **105,** 13239–13252 .

Manrı́quez, P., Contreras-Reyes, E. & Osses, A., 2014. Lithospheric 3-D flexure modelling of the oceanic plate seaward of the trench using variable elastic thickness, *Geophys. J. Int.,* **196**(2), 681–693.

Masson, D.G., 1991. Fault patterns at outer trench walls, *Mar. Geophys. Res.,* **13,** 209–225.

McAdoo, D.C., Martin, C.F. & Poulose, S., 1985. Seasat observations of flexure: Evidence for a strong lithosphere, *Tectonophysics,* **116,** 209–222.

McIntosh, K., van Avendonk, H.J.A., Lavier, L., Lester, W. R., Eakin, D., Wu, F., Liu, C.-S. & Lee, C.-S., 2013. Inversion of a hyper-extended rifted margin in the southern Central Range of Taiwan, *Geology,* **41**(8), 871–874.

McNutt, M.K., 1984. Lithospheric flexure and thermal anomalies, *J. geophys. Res.,* **89,** 11 180–11 194.

Mcnutt, M.K., Diament, M. & Kogan, M.G., 1988. Variations of elastic plate thickness at continental thrust belts, *J. geophys. Res.,* **93,** 8825–8838.

McQueen, H.W.S. & Lambeck, K., 1989. The accuracy of some lithospheric bending parameters, *Geophys. J. Int.,* **96,** 401–413.

Mei, S., Suzuki, A.M., Kohlstedt, D.L., Dixon, N.A. & Durham, W.B., 2010. Experimental constraints on the strength of the lithospheric mantle, *J. geophys. Res.,* **115**(B8).

Melosh, H.J., 1978. Dynamic support of the outer rise, *Geophys. Res. Lett.,* **5**(5), 321–324.

Mortera-Gutiérrez, C.A., Scholl, D.W. & Carlson, R.L., 2003. Fault trends on the seaward slope of the Aleutian Trench: Implications for a laterally hanging stress field tied to a westward increase in oblique convergence, *J. geophys. Res.,* **108,** 2477.

Mouthereau, F. & Petit, C., 2003. Rheology and strength of the Eurasian continental lithosphere in the foreland of the Taiwan collision belt: constraints from seismicity, flexure, and structural styles, *J. geophys. Res.,* **108**(B11).

Muller, S., Choy, G.L. & Spence, W., 1996. Inelastic models of lithospheric stress—I. Theory and application to outer-rise plate deformation, *Geophys. J. Int.,* **125,** 39–53.

Oakley, A.J., Taylor, B. & Moore, G.F., 2008. Pacific Plate subduction beneath the central Mariana and Izu-Bonin fore arcs: new insights from an old margin, *Geochem. Geophys. Geosyst.,* **9,** 6.

Panteleyev, A.N. & Diament, M., 1993. Influence of some rheological parameters on flexure of the oceanic lithosphere, *Geophys. J. Int.,* **114,** 209–220.

Parsons, B. & Molnar, P., 1976. The origin of outer topographic rises associated with trenches, *Geophys. J. Int.,* **1**(4), 707–712.

Parsons, B. & Sclater, J.G., 1977. An analysis of the variation of oceanic floor bathymetry and heat flow with age, *J. geophys. Res.,* **82**: 803–827.

Ranero, C.R., Morgan, J.P., McIntosh, K. & Reichert, C., 2003. Bending-related faulting and mantle serpentinization at the Middle America trench, *Nature,* **425**(6956), 367–373.

Ranero, C.R., Villaseñor, A., Morgan, J.P. & Weinrebe, W., 2005. Relationship between bend-faulting at trenches and intermediate-depth seismicity, *Geochem.Geophys.Geosyst*., **6**(12).

Rangin, C., Le Pichon, X., Mazzotti, S., Pubellier, M., Chamot-Rooke, N., Aurelio, M., Walpersdorf, A. & Quebral, R., 1999. Plate convergence measured by GPS across the Sundaland/Phillippine Sea Plate deformed boundary: the Phillippines and eastern Indonesia, *Geophys. J. Int.,* **139,** 296–316.

Raterron, P., Wu, Y., Weidner, D.J. & Chen, J., 2004. Low-temperature olivine rheology at high pressure, *Phys. Earth planet. Inter.,* **145**(1), 149–159.

Seno, T., Stein, S. & Gripp, A. E., 1993. A model for the motion of the Philippine Sea plate consistent with NUVEL-I and geologic data, *J. geophys. Res.,* **98,** 17941–17948.

Shi, Y.-H. & Eberhart, R.C., 1998. A modified particle swarm optimizer, *Proceeding of the IEEE International Conference on Evolutionary Computation,* 69–73.

Taylor, B. & Hayes, D. E., 1983. Origin and history of the South China Sea basin, in *The Tectonic and Geologic Evolution of Southeast Asian Seas and Islands: Part 2, Geophys. Monogr. Ser.,* vol. **27,** pp. 23–56, ed. Hayes, D.E., AGU.

Tensi, J., Mouthereau, F. & Lacombe, O., 2006. Lithospheric bulge in the West Taiwan Basin, *Basin Res.,* **18,** 277–299.

Timoshenko, S. & Woinowsky-Krieger, S., 1959. *Theory of plates and shells,* 2nd, McGraw-Hill, New York, p. 568.

Turcotte, D., McAdoo, D. & Caldwell, J., 1978. An elastic-perfectly plastic analysis of the bending of the lithosphere at a trench, *Tectonophysics,* **47**(3–4), 193–205.

Turcotte, D. & Schubert, G., 2014. *Geodynamics,* 3nd edn. Cambridge University Press, pp. 626.

van Wees, J. & Cloetingh, S., 1994. A finite difference technique to incorporate spatial variations in rigidity and planar faults into 3-D models for lithospheric flexure, *Geophys. J. Int.,* **117,** 179–195.

Wang, W.-H. & Lee, Y.-H., 2011. 3-D plate interactions in central Taiwan: Insight from flexure and sandbox modeling, *Earth planet. Sci. Lett.,* **308,** 1–11.

Watts, A.B., 1978. An analysis of Isostasy in the world's oceans: 1.Hawaiian-Emperor seamount Chain, *J. geophys. Res.,* **83,** 5989–6004.

Watts, A.B., 2001. *Isostasy and Flexure of the Lithosphere,* 1st edn, Cambridge University Press, New York, p. 478.

Watts, A.B. & Talwani, M., 1974. Gravity anomalies seaward of deep-sea trenches and their tectonic implications, *Geophys. J. Int.,* **36**(1), 57–90.

Wessel, P., 1996. Analytical solutions for 3-D flexural deformation of semi-infinite elastic plates, *Geophys. J. Int.,* **124**(3), 907–918.

Wessel, P. & Smith, W.H.F., 1998. New, improved version of generic mapping tools released, *Eos Transactions,* **79,** 579–579.

Zhang, F., Lin, J. & Zhan, W.-H., 2014. Variations in oceanic plate bending along the Mariana Trench, *Earth planet. Sci. Lett.,* **401,** 206–214.

Zhang, F., Lin, J., Zhou, Z.Y., Yang, H.F. & Zhan, W.H., 2018. Intra- and inter-trench variations in flexural bending of the Manila, Mariana and global trenches: Implications on plate weakening in controlling trench dynamics, *Geophys. J. Int.,* **212,** 1429–1449.

Zhou, Z.-Y. & Lin, J., 2018. Elasto- plastic deformation and plate weakening due to normal faulting in the subducting plate along the Mariana Trench, *Tectonophysics,* **734,** 59–68.

Zhou, Z.-Y., Lin, J., Behn, M.D. & Olive, J.A., 2015. Mechanism for normal faulting in the subducting plate at the Mariana Trench, *Geophys. Res. Lett.,* **42,** 4309–4317.

APPENDIX: FLEXURAL MODELLING

The flexure of the lithosphere floating on an inviscid layer (asthenosphere) is governed by the partial differential equation (eq. 1), in which the derivative terms can be re-written using the following centred finite difference operators at a point (i) with regular spacings Δx and Δy:

$$\begin{aligned}
&\left.\frac{\partial w}{\partial x}\right|(i) \approx \frac{w(i+1)-w(i-1)}{2\Delta x}\\
&\left.\frac{\partial w}{\partial y}\right|(i) \approx \frac{w(i-m)-w(i+m)}{2\Delta y}\\
&\left.\frac{\partial^2 w}{\partial x^2}\right|(i) \approx \frac{w(i+1)-2w(i)+w(i-1)}{\Delta x^2}\\
&\left.\frac{\partial^2 w}{\partial y^2}\right|(i) \approx \frac{w(i-m)-2w(i)+w(i+m)}{\Delta y^2}\\
&\left.\frac{\partial^2 w}{\partial x\partial y}\right|(i) \approx \frac{w(i-m+1)+w(i+m-1)-w(i-m-1)-w(i+m+1)}{4\Delta x\Delta y}\\
&\left.\frac{\partial^3 w}{\partial x^3}\right|(i) \approx \frac{w(i+2)-2w(i+1)+w(i-1)-w(i-2)}{2\Delta x^3}\\
&\left.\frac{\partial^3 w}{\partial y^3}\right|(i) \approx \frac{w(i-2m)-2w(i-m)+2w(i+m)-w(i+2m)}{2\Delta y^3}\\
&\left.\frac{\partial^3 w}{\partial x\partial y^2}\right|(i) \approx \frac{w(i+m+1)+w(i-m+1)-w(i-m-1)-w(i+m-1)+2w(i-1)-2w(i+1)}{2\Delta x\Delta y^2}\\
&\left.\frac{\partial^3 w}{\partial x^2\partial y}\right|(i) \approx \frac{w(i-m-1)+w(i-m+1)-w(i+m+1)-w(i+m-1)+2w(i+m)-2w(i-m)}{2\Delta x^2\Delta y}\\
&\left.\frac{\partial^4 w}{\partial x^4}\right|(i) \approx \frac{6w(i)-4[w(i+1)+w(i-1)]+w(i+2)+w(i-2)}{\Delta x^4}\\
&\left.\frac{\partial^4 w}{\partial y^4}\right|(i) \approx \frac{6w(i)-4[w(i+m)+w(i-m)]+w(i+2m)+w(i-2m)}{\Delta y^4}\\
&\left.\frac{\partial^4 w}{\partial x^2\partial y^2}\right|(i) \approx \frac{4w(i)-2[w(i+1)+w(i-1)+w(i+m)+w(i-m)]+w(i+m+1)+w(i-m+1)+w(i-m-1)+w(i+m-1)}{\Delta x^2\Delta y^2}.
\end{aligned} \tag{A1}$$

Here we use (i), rather than (i, j) to represent the sequence number of nodes, which makes programming easier. i is from 1 to $n \times m$ (The square are divided into n rows and m column). It shows that each point (i) of the regular grid connects to its 12 closest neighbours (Fig. A1). The derivative terms of flexural rigidity D can be also rewritten by the centred finite difference operators with regular spacings Δx and Δy:

$$\begin{aligned}
D_x &= \left.\frac{\partial D}{\partial x}\right|(i) \approx \frac{D(i+1)-D(i-1)}{2\Delta x}\\
D_y &= \left.\frac{\partial D}{\partial y}\right|(i) \approx \frac{D(i-m)-D(i+m)}{2\Delta y}\\
D_{xx} &= \left.\frac{\partial^2 D}{\partial x^2}\right|(i) \approx \frac{D(i+1)-2D(i)+D(i-1)}{\Delta x^2}\\
D_{yy} &= \left.\frac{\partial^2 D}{\partial x^2}\right|(i) \approx \frac{D(i-m)-2D(i)+D(i+m)}{\Delta y^2}\\
D_{xy} &= \left.\frac{\partial^2 D}{\partial x\partial y}\right|(i) \approx \frac{D(i-m+1)+D(i+m-1)-D(i-m-1)-D(i+m+1)}{\Delta x\Delta y}
\end{aligned} \tag{A2}$$

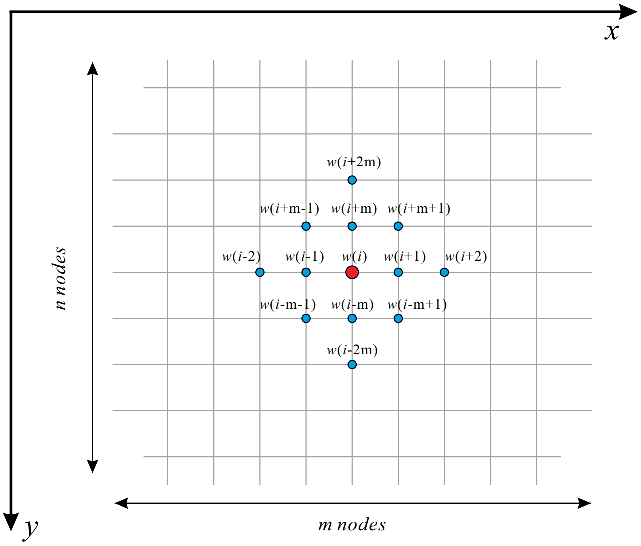

Figure A1. Sketch map of the finite difference scheme.

The eq. (1) reduces to a set of coupled linear equations, which can be expressed as matrix form: **AW = Q** (eq. 7). **A** is the coefficient matrix, **W** is the vector of unknown deflection w and **Q** is the loading vector, respectively, given by:

$$
\boldsymbol{A}=\begin{bmatrix}
A_{i-2m} \\
& \ddots \\
&& A_{i-m-1} \\
&&& A_{i-m} \\
&&&& A_{i-m+1} \\
&&&&& \ddots \\
&&&&&& A_{i-2} \\
&&&&&&& A_{i-1} \\
&&&&&&&& A_{i} \\
&&&&&&&&& A_{i+1} \\
&&&&&&&&&& A_{i+2} \\
&&&&&&&&&&& \ddots \\
&&&&&&&&&&&& A_{i+m-1} \\
&&&&&&&&&&&&& A_{i+m} \\
&&&&&&&&&&&&&& A_{i+m+1} \\
&&&&&&&&&&&&&&& \ddots \\
&&&&&&&&&&&&&&&& A_{i+2m}
\end{bmatrix}
$$

$$
\boldsymbol{W}=\left[\, w_{i-2m} \ \ldots \ w_{i-m-1} \ w_{i-m} \ w_{i-m+1} \ \cdots \ w_{i-2} \ w_{i-1} \ w_{i} \ w_{i+1} \ w_{i+2} \ \cdots \ w_{i+m-1} \ w_{i+m} \ w_{i+m+1} \ \cdots \ w_{i+2m} \,\right]^{T}
$$

$$
\boldsymbol{Q}=\left[\, q_{i-2m} \ \ldots \ q_{i-m-1} \ q_{i-m} \ q_{i-m+1} \ \cdots \ q_{i-2} \ q_{i-1} \ q_{i} \ q_{i+1} \ q_{i+2} \ \cdots \ q_{i+m-1} \ q_{i+m} \ q_{i+m+1} \ \cdots \ q_{i+2m} \,\right]^{T} \tag{A3}
$$

$$
\begin{aligned}
A_{i-2m} &= \frac{D_y}{\Delta y^3} + \frac{D}{\Delta y^4} \\
A_{i-m-1} &= -\frac{D_x}{\Delta x \Delta y^2} + \frac{D_y}{\Delta x^2 \Delta y} - \frac{D_{xy}(1-v)}{2\Delta x \Delta y} + \frac{2D}{\Delta x^2 \Delta y^2} + \frac{N_{xy}}{2\Delta x \Delta y} \\
A_{i-m} &= \frac{vD_{xx} + D_{yy}}{\Delta y^2} - 2D_y\left(\frac{1}{\Delta y^3} + \frac{1}{\Delta x^2 \Delta y}\right) - \frac{4D}{\Delta y^2}\left(\frac{1}{\Delta y^2} + \frac{1}{\Delta x^2}\right) - \frac{N_{yy}}{\Delta y^2} \\
A_{i-m+1} &= \frac{D_x}{\Delta x \Delta y^2} + \frac{D_y}{\Delta x^2 \Delta y} + \frac{D_{xy}(1-v)}{2\Delta x \Delta y} + \frac{2D}{\Delta x^2 \Delta y^2} - \frac{N_{xy}}{2\Delta x \Delta y} \\
A_{i-2} &= -\frac{D_x}{\Delta x^3} + \frac{D}{\Delta y^4} \\
A_{i-1} &= \frac{D_{xx} + vD_{yy}}{\Delta x^2} + 2D_x\left(\frac{1}{\Delta x^3} + \frac{1}{\Delta x \Delta y^2}\right) - \frac{4D}{\Delta x^2}\left(\frac{1}{\Delta x^2} + \frac{1}{\Delta y^2}\right) - \frac{N_{xx}}{\Delta x^2} \\
A_i &= -2D_{xx}\left(\frac{1}{\Delta x^2} + \frac{v}{\Delta y^2}\right) - 2D_{yy}\left(\frac{1}{\Delta y^2} + \frac{v}{\Delta x^2}\right) + 6D\left(\frac{1}{\Delta x^4} + \frac{1}{\Delta y^4}\right) + \frac{8D}{\Delta x^2 \Delta y^2} + \frac{2N_{xx}}{\Delta x^2} + \frac{2N_{yy}}{\Delta y^2} + \Delta\rho g \\
A_{i+1} &= \frac{D_{xx} + vD_{yy}}{\Delta x^2} - 2D_x\left(\frac{1}{\Delta x^3} + \frac{1}{\Delta x \Delta y^2}\right) - \frac{4D}{\Delta x^2}\left(\frac{1}{\Delta x^2} + \frac{1}{\Delta y^2}\right) - \frac{N_{xx}}{\Delta x^2} \\
A_{i+2} &= \frac{D_x}{\Delta x^3} + \frac{D}{\Delta x^3} \\
A_{i+m-1} &= -\frac{D_x}{\Delta x \Delta y^2} - \frac{D_y}{\Delta x^2 \Delta y} + \frac{D_{xy}(1-v)}{2\Delta x \Delta y} + \frac{2D}{\Delta x^2 \Delta y^2} - \frac{N_{xy}}{2\Delta x \Delta y} \\
A_{i+m} &= \frac{vD_{xx} + D_{yy}}{\Delta y^2} + 2D_y\left(\frac{1}{\Delta y^3} + \frac{1}{\Delta x^2 \Delta y}\right) - \frac{4D}{\Delta y^2}\left(\frac{1}{\Delta y^2} + \frac{1}{\Delta x^2}\right) - \frac{N_{yy}}{\Delta y^2} \\
A_{i+m+1} &= \frac{D_x}{\Delta x \Delta y^2} - \frac{D_y}{\Delta x^2 \Delta y} - \frac{D_{xy}(1-v)}{2\Delta x \Delta y} + \frac{2D}{\Delta x^2 \Delta y^2} + \frac{N_{xy}}{2\Delta x \Delta y} \\
A_{i+2m} &= -\frac{D_y}{\Delta y^3} + \frac{D}{\Delta y^4}.
\end{aligned} \tag{A4}
$$

Following this, nodes at all boundary conditions can be also rewritten by finite difference operators. **W** then can be solved according to the combination of eqs (A1)–(A4) and boundary conditions.